

Implications for Galactic Electron Density Structure from Pulsar Sightlines Intersecting H II Regions

STELLA KOCH OCKER ^{1,2}, LOREN D. ANDERSON ³, JOSEPH LAZIO⁴, JAMES M. CORDES ⁵ AND VIKRAM RAVI ^{1,6}

¹*Cahill Center for Astronomy and Astrophysics, California Institute of Technology, Pasadena, CA 91125, USA*

²*The Observatories of the Carnegie Institution for Science, Pasadena, CA 91101, USA*

³*Department of Physics and Astronomy, West Virginia University, Morgantown, WV 26506, USA*

⁴*Jet Propulsion Laboratory, California Institute of Technology, Pasadena, CA 91106, USA*

⁵*Department of Astronomy and Cornell Center for Astrophysics and Planetary Science, Cornell University, Ithaca, NY, 14853, USA*

⁶*Owens Valley Radio Observatory, California Institute of Technology, Big Pine, CA 93513, USA*

Submitted to The Astrophysical Journal

ABSTRACT

Recent radio surveys have revealed pulsars with dispersion and scattering delays induced by ionized gas that are larger than the rest of the observed pulsar population, in some cases with electron column densities (or dispersion measures; DMs) larger than the maximum predictions of Galactic electron density models. By cross-matching the observed pulsar population against H II region catalogs, we show that the majority of pulsars with $DM > 600 \text{ pc cm}^{-3}$ and scattering delays $\tau(1 \text{ GHz}) > 10 \text{ ms}$ lie behind H II regions, and that H II region intersections may be relevant to as much as a third of the observed pulsar population. Accounting for H II regions resolves apparent discrepancies where Galactic electron density models place high-DM pulsars beyond the Galactic disk. By comparing emission measures (EMs) inferred from recombination line observations to pulsar DMs, we show that H II regions can contribute tens to hundreds of pc cm^{-3} in electron column density along a pulsar LOS. We find that nearly all pulsars with significant excess (and deficit) scattering from the mean τ -DM relation are spatially coincident with known discrete ionized gas structures, including H II regions. Accounting for H II regions is critical to the interpretation of radio dispersion and scattering measurements as electron density tracers, both in the Milky Way and in other galaxies.

Keywords: ISM:general –pulsars –radio transients –H II regions –scattering –turbulence

1. INTRODUCTION

The Milky Way interstellar medium (ISM) contains a range of ionized structures, from highly dense H II regions enshrouding ultraviolet stars and tenuous hot bubbles evacuated by supernovae (SNe), to the diffuse, warm ionized medium that extends both across and beyond the Galactic plane. The distribution of this multi-phase gas is a critical tracer of star formation and stellar feedback, and their role in sculpting our Galaxy. Radio pulsars are sensitive probes of ionized gas, which causes dispersion, scattering, and birefringence manifesting as frequency-dependent time delays and intensity modulations in observed radio pulses. Accounting for these propagation effects is critical to pulsar timing experiments (Agazie et al. 2023; EPTA Collaboration et al. 2023; Reardon

et al. 2023), in addition to serving as input to Galactic electron density models that predict distances to both Galactic and extragalactic radio sources (Cordes et al. 1991; Cordes & Lazio 2002; Yao et al. 2017).

Recently, high-sensitivity pulsar surveys with MeerKAT and the Five-hundred-meter Aperture Spherical radio Telescope (FAST) have unveiled pulsars in the Galactic plane with dispersion and scattering delays larger than the rest of the known population (Johnston et al. 2020; Oswald et al. 2021; Han et al. 2021; Posselt et al. 2023). In some cases, the pulse dispersion measure ($DM = \int_0^D n_e dl$, where n_e is electron density and D is the pulsar distance) is larger than the maximum DMs predicted by Galactic electron density models NE2001 (Cordes & Lazio 2002, 2003) and YMW16 (Yao et al. 2017), implying that these pulsars either lie beyond the Galactic disk or that the models are missing a significant portion of the ISM’s free electrons along these lines-of-sight (LOSs). The FAST Galactic Plane Pulsar Survey (GPPS) has thus far identified ~ 10 pulsars with DMs larger

than Galactic model predictions that are spatially coincident with H II regions, suggesting that these H II regions may explain the apparent DM excess (Han et al. 2021).

H II regions can dramatically influence pulsar propagation observables by enhancing dispersion, scattering, and Faraday rotation, which are all LOS-integrated effects. Based on their DMs and rotation measures (RMs), pulsars have been used to infer mean electron densities $\approx 10 \text{ cm}^{-3}$ (Ocker et al. 2020) and magnetic field magnitudes $\approx 6 \mu\text{G}$ (Harvey-Smith et al. 2011) within H II regions. Localization of pulsar scattering to H II regions suggests that density fluctuations within those regions are moderately enhanced relative to the warm ionized ISM (Ocker et al. 2020; Mall et al. 2022; Ocker et al. 2024) and may be consistent with a turbulence cascade that dissipates at an inner scale $\approx 70 - 100 \text{ km}$ (Rickett et al. 2009). Unambiguously making such inferences for individual H II regions requires knowledge of both the pulsar and H II region distances, and is hindered by the limited pulsar distance sample and the large kinematic uncertainties of many H II region distances. Constraints on ionized gas elsewhere along the pulsar LOS are also generally required, based on examination of other pulsars at similar locations and/or analysis of complementary multi-wavelength surveys sensitive to diffuse ionized gas. As such, pulsars have been used to probe the internal properties of H II regions in only a select handful of cases (e.g. Mitra et al. 2003; Harvey-Smith et al. 2011; Ocker et al. 2020), even though H II regions have long been invoked as a potential explanation for enhanced DM and scattering in the inner Galaxy (Spangler 1991; McKee & Williams 1997).

In this study, we leverage expansive H II region catalogs to perform a large-scale comparison between the Galactic distribution of H II regions and the pulsar population. Such a comparison is now fruitful due largely to the $> 2\times$ increase in the number of both known and likely H II regions over the past decade, chiefly thanks to infrared (IR) and radio surveys sensitive to H II regions across the entire Galactic plane (Bania et al. 2010; Anderson et al. 2014; Wenger et al. 2021) and a concurrent increase in the known Galactic pulsar population. We employ two large H II region catalogs, the WISE Catalog (Anderson et al. 2014), so called for its use of the Wide-Field Infrared Survey Explorer (Wright et al. 2010), and Hou & Han (2014), hereafter HH14, which together contain ≈ 8500 H II regions identified at IR, radio, and/or optical wavelengths, of which ≈ 3000 have measured distances. Despite uncertainties in both pulsar and H II region distances, we are able to identify hundreds of pulsars that likely intersect H II regions, of which ~ 100 pulsars have both DM and scattering measurements. We assess the impact of these H II regions on pulsar observations through both a statistical analysis of the sample, and through detailed investigation of specific regions.

The paper is organized as follows: Section 2 introduces the H II region catalogs and their distance measurements. Section 3 describes the methodology used to identify pulsars intersecting these H II regions and describes the number and validity of intersections. In Section 4 we discuss general trends in the radio properties of pulsars intersecting H II regions, and in Section 5 we compare pulsar properties to radio recombination line observations of specific regions based on the Green Bank Diffuse Ionized Gas Survey (GDIGS; Anderson et al. 2021), FAST GPPS (Hou et al. 2022), and the Sino-German 6 cm Survey (SGS; Gao et al. 2019). Section 6 uses pulsar scattering measurements to constrain the strength of electron density fluctuations within H II regions. Implications for Galactic electron density models and their applications are discussed in Section 7, and conclusions are summarized in Section 8.

2. GALACTIC H II REGION CATALOGS

While H II regions were first identified in large numbers by their optical emission (Gum 1955; Sharpless 1959), modern catalogs have leveraged IR and radio surveys to discover thousands of H II regions that are not detected at optical wavelengths due to the severe visual extinction at their relatively large distances. We employ two comprehensive H II region catalogs, the WISE Catalog (v2.3, Anderson et al. 2014) and HH14 (Hou & Han 2014), which encompass H II region detections across optical, IR, and radio wavelengths. A subset of these H II regions have distance measurements described further below, and which form the primary sample that we compare to pulsar LOSs. Sources in the WISE Catalog were selected from IR data, spanning all Galactic longitudes and latitudes $|b| \leq 8^\circ$. The sources were cross-matched with known H II regions and in the process known H II regions at higher (and lower) absolute latitudes were added. By contrast, HH14 is a compilation of H II region detections from the published literature, based on surveys spanning a range of wavelengths, sensitivities, and sky coverages. The overlap between H II regions with distances cataloged in WISE and HH14 is incomplete, in part because HH14 includes spectrophotometric distances whereas WISE does not. In order to make use of as many H II region distances as possible, we use both catalogs and account for their overlap in subsequent analyses (§3). Many of the kinematic distances we use originate from sources adopting different Galactic rotation curves. While re-deriving kinematic distances for the entire H II region sample using a single Galactic rotation curve is beyond the scope of this work, we note that the differences between kinematic distances derived from different rotation curve parameters are typically comparable to or smaller than most kinematic distance uncertainties (e.g. Hou & Han 2014). Each catalog is described in turn below and is available on the Vizier catalog service (Ochsenbein

et al. 2000); for the latest version of the WISE Catalog, see <http://astro.phys.wvu.edu/wise/>.

2.1. WISE Catalog

The WISE Catalog consists of ≈ 8400 H II regions detected using IR data from the WISE and Spitzer space telescopes. WISE and Spitzer can detect H II regions across the entire Galaxy due to a combination of low extinction and high sensitivity. Centroid positions and angular sizes for the H II regions are provided by the catalog based on the IR data (in contrast to HH14, which only provides centroids). The catalog is estimated to be complete for all H II regions ionized by O-stars, and likely has a high completeness fraction for stellar types B0-B2 (Anderson et al. 2014; Armentrout et al. 2021). The mid-IR emission is from heated dust and exhibits a characteristic morphology consisting of $\sim 20 \mu\text{m}$ emission surrounded by $\sim 10 \mu\text{m}$ emission that coincides with radio continuum emission (Anderson et al. 2012). In practice, H II region morphologies are complex and varied (see e.g. Wood & Churchwell 1989), and they can be confused with planetary nebulae and external galaxies if their spectral energy distributions are not taken into account. The WISE Catalog excludes such interlopers where possible based on cross-matches with both known objects and surveys of recombination lines, which are unambiguous identifiers of H II regions. About 2000 H II regions in the WISE Catalog are classified as “known” based on cross-matching with the Fich et al. (1990) $\text{H}\alpha$ emission catalog covering the Northern hemisphere and via radio recombination line (RRL) observations (Caswell & Haynes 1987; Lockman 1989; Lockman et al. 1996; Bania et al. 2010, 2012; Anderson et al. 2015; Alves et al. 2015; Anderson et al. 2018; Liu et al. 2019; Wenger et al. 2021). These recombination line observations imply that $< 5\%$ of sources in the WISE Catalog classified as “candidates” (corresponding to positive detection of IR and radio continuum emission) are not bona fide H II regions (Anderson et al. 2011), and that $> 50\%$ of sources classified in the WISE Catalog as “radio-quiet” (only IR detections to date) are bona fide H II regions (Armentrout et al. 2021).

The latest release of the WISE Catalog includes ≈ 2800 distances, with nearly 400 of those distances based on parallax and the rest kinematic. The most accurate distance determinations are from maser parallaxes, many provided by Reid et al. (2019). Kinematic distances include those based on RRL radial velocities measured by the H II Region Discovery Survey (Wenger et al. 2021). Kinematic distances have substantial uncertainties, with inner Galaxy LOSs yielding both near and far possible solutions. Anderson et al. (2014) break the kinematic distance ambiguity (KDA) where possible using emission and absorption of HI and H_2CO (e.g. Dunham et al. 2011; Urquhart et al. 2011, 2012), and if the H II region is detected optically, e.g. in $\text{H}\alpha$ emission, the near distance is

adopted. Even when the KDA is broken, kinematic distances can still have uncertainties of up to a few kiloparsecs. For cases where the KDA is not resolved, we adopt the near distance as a lower limit and the far distance as an upper limit. We ignore near kinematic distances < 0.1 kpc, which lead to many spurious pulsar intersections.

2.2. HH14 Catalog

The HH14 Catalog provides 4550 spectral line measurements towards 2540 H II regions, of which about 1870 have distance measurements. HH14 is a compilation of primarily optical and radio detections from the literature, including a large fraction of RRLs that were also included in the WISE Catalog. The catalog does not include most of the IR-only candidates identified with WISE, but it does provide spectrophotometric distances in addition to kinematic and parallax distances, thereby increasing the total sample of H II region distances at our disposal. HH14 also includes distances for several large, high-latitude H II regions without distances in the WISE Catalog (e.g. S7, S27). Spectrophotometric distances are based on identification of the main ionizing star and its spectral type, with associated uncertainties arising from a combination of misidentification of the ionizing star, spectral (mis)-classification, photometric errors, spread in the stellar luminosity of a given spectral type, and the assumed reddening law (e.g. Foster & Brunt 2015). The impact of these distance uncertainties on our analysis is considered in Section 3.2. All sources in HH14 have ionized gas line measurements, and we thus expect nearly all sources in HH14 are bona fide H II regions.

3. PULSARS INTERSECTING H II REGIONS

We first describe the methodology used to identify H II region intersections, followed by a summary of the intersection candidates identified and our assessment of their validity.

3.1. Methodology

We identify pulsars intersecting H II regions using three key parameters: the pulsar and H II region sky positions, distances, and the H II region size. We compare the pulsar population to the WISE and HH14 catalogs independently, and then merge the results to produce a single unique list of intersections.

For the WISE Catalog cross-match, we exclude pulsars with projected offsets $> 2\theta_{\text{IR}}$ away from the H II region centroid position, where θ_{IR} is the angular radius of the IR emission provided by the WISE Catalog. The maximum projected offset (i.e., the maximum impact parameter) is larger than the IR angular size because the exact physical extent of the ionized gas is not known a priori, and the IR angular size may be an underestimate of the ionized gas extent due to radiation leakage that ionizes the outer envelope of the H II region

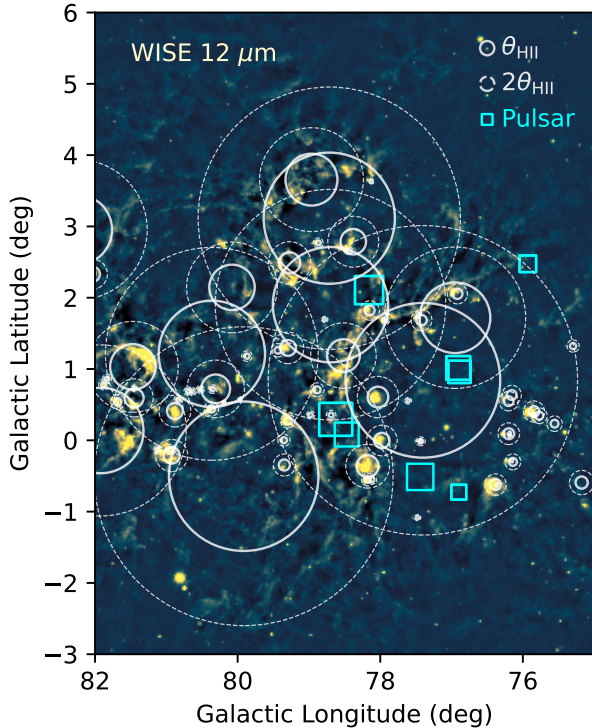


Figure 1. Illustration of the identification of pulsars likely behind H II regions. The background is a WISE $12\ \mu\text{m}$ image. White circles are for H II regions for which there are estimated distances, with the sizes of the circles based on their θ_{IR} in the WISE Catalog. Large white circles that appear to be devoid of $12\ \mu\text{m}$ emission are brighter at $20\ \mu\text{m}$ and identified as H II regions on that basis. Cyan squares indicate pulsars identified as lying behind an H II region based on the criteria described in Section 3.1. The sizes of the squares indicate the relative magnitudes of the pulsar DMs, with larger squares corresponding to larger DMs.

(e.g. [Luisi et al. 2019](#)). HH14 does not provide the H II region angular sizes, so we set the maximum impact parameter to 20 pc, re-scaled to an angular size based on the H II region distance. This projected offset is the minimum value that reproduces known H II region intersections from [Mitra et al. \(2003\)](#), [Harvey-Smith et al. \(2011\)](#), and [Ocker et al. \(2020\)](#), which are cases where the pulsar and H II region distances are known and the pulsar location is spatially coincident with the H II region in $H\alpha$ emission maps. An impact parameter cut-off of 20 pc corresponds roughly to the expected Strömgren radii of H II regions around star types O8-O9 and B0, suggesting that our analysis may miss intersections through H II regions around early-type O-stars ([Rubin 1968](#)). The incompleteness fraction of our intersection analysis is assessed further in Section 3.2. Figure 1 shows an example of intersections through an H II region complex in the WISE Catalog, identified using our selection criteria.

We only search for intersections through the ≈ 3000 H II regions with distance measurements, but we consider all ra-

dio pulsars in the ATNF Catalog (v2.1.1, [Manchester et al. 2005](#))¹. Only about 300 pulsars have distance measures, half of which are parallax² (e.g., [Deller et al. 2019](#); [Ding et al. 2023](#)) and the rest based on either H I kinematics or associations (e.g., [Frail & Weisberg 1990](#); [Pan et al. 2021](#)). For pulsars without distance measures, we use Python implementations of NE2001 ([Cordes & Lazio 2002, 2003](#); [Ocker & Cordes 2024](#)) and YMW16 ([Yao et al. 2017](#); [Price et al. 2021](#)) to estimate their distances based on observed DMs, and we classify the pulsar LOS as intersecting an H II region if at least one of the models predicts a pulsar distance greater than the H II region distance, with the following caveats: For the sample of pulsars with known distances, these Galactic electron density models typically misestimate distances by $\approx 30\%$ ([Price et al. 2021](#)), although for some pulsar LOSs the models misestimate the distance by $\gtrsim 100\%$ due to discrete, unmodeled density structures, including H II regions ([Ocker et al. 2020](#); [Ding et al. 2023](#)). While NE2001 models H II regions for select LOSs on an ad hoc basis, YMW16 does not model H II regions at all. When a pulsar does intersect an H II region that is not included in the models, they will generally overestimate the pulsar distance because they have to integrate to larger distances to reproduce the observed DM. In these cases, the uncertainty in the model distance does not impact our ability to identify H II region intersections. Nonetheless, the combination of uncertainties on both pulsar and H II region distances implies that we expect some false intersection candidates and some intersections that are missed altogether, and we attempt to identify these false positives and negatives where possible (§3.2).

The intersection analysis is performed for two pulsar samples, the entire known radio pulsar population (~ 3000 pulsars), and a subset of ≈ 500 pulsars with scattering measurements. The first, bulk pulsar sample is used to statistically compare the DM distribution of intersection candidates against that of the broader pulsar population. The second sample of pulsars with scattering measurements is used for detailed analysis, where the sample is small enough to individually assess the validity of each intersection candidate based on the transverse proximity of the pulsar LOS to the H II region and the difference between the pulsar’s estimated distance and that of the H II region (see below).

3.2. Intersection Candidates

The initial cross-match between all known radio pulsars and the H II regions with distances in the WISE and HH14 catalogs yields 660 intersection candidates, where intersections are taken to be impact parameters $< 2\theta_{\text{IR}}$ for H II regions in the WISE Catalog or 20 pc for H II regions in HH14.

¹ <http://www.atnf.csiro.au/research/pulsar/psrcat>

² <https://hosting.astro.cornell.edu/research/parallax/>

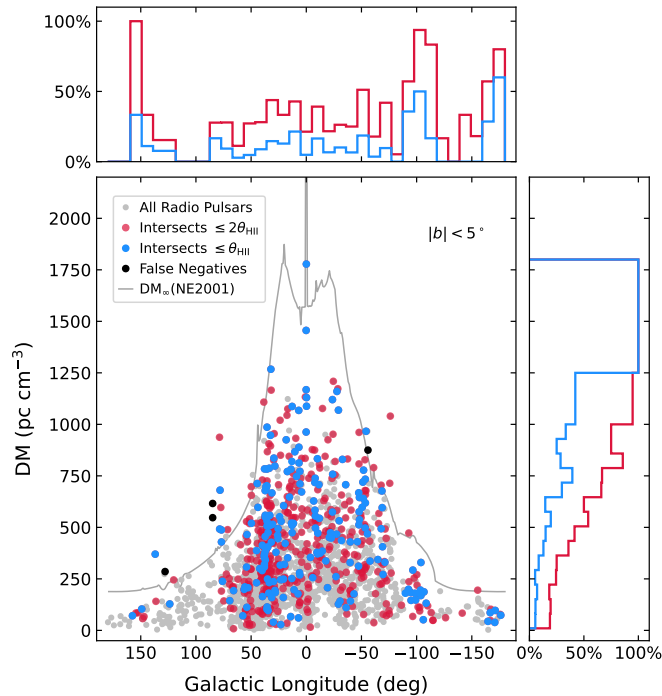


Figure 2. DM vs. Galactic longitude for all radio pulsars at Galactic latitudes $|b| < 5^\circ$ (grey points) and for pulsars intersecting H II regions with measured distances. Red points indicate pulsars that pass within $2\theta_{\text{HII}}$ of a known H II region, where θ_{HII} is the angular radius provided by WISE, assumed to be 10 pc for H II regions in HH14 (corresponding to a nominal impact parameter cutoff $2\theta_{\text{HII}} = 20$ pc; §3). Blue points are pulsars within θ_{HII} . The thin grey line indicates the maximum DM predicted by NE2001 at $b = 0^\circ$. Black points indicate pulsars with large DMs that do intersect H II regions but were missed by our selection criteria (false negatives). The top and side panels show the fraction of all low-latitude pulsars that intersect H II regions within $2\theta_{\text{HII}}$ (red lines) and θ_{HII} (blue lines).

About 220 (33%) of these intersections are within half the impact parameter cutoff (θ_{IR} for the WISE Catalog or 10 pc for HH14), but this more restrictive cutoff excludes a number of pulsars that intersect H II region complexes with extended emission beyond the IR angular radii recorded in the WISE Catalog. Figure 2 shows the distribution of DM vs. Galactic longitude for the H II region intersections identified with both impact parameter cutoffs; this figure is discussed further in Section 4. We estimate a false positive rate of $\approx 20\%$ for spurious intersections (see below).

We identify 107 intersections where the pulsar has a published scattering measurement. We build upon the compilation of scattering measurements from Cordes et al. (2016, 2022), which encompasses ≈ 500 pulsars that have either pulse broadening times and/or scintillation bandwidths reported in the literature, by adding scattering times we have inferred from pulse profiles released by FAST GPPS (Han et al. 2021). The list of H II region intersections is shown in Table A1, including both pulsar and H II region prop-

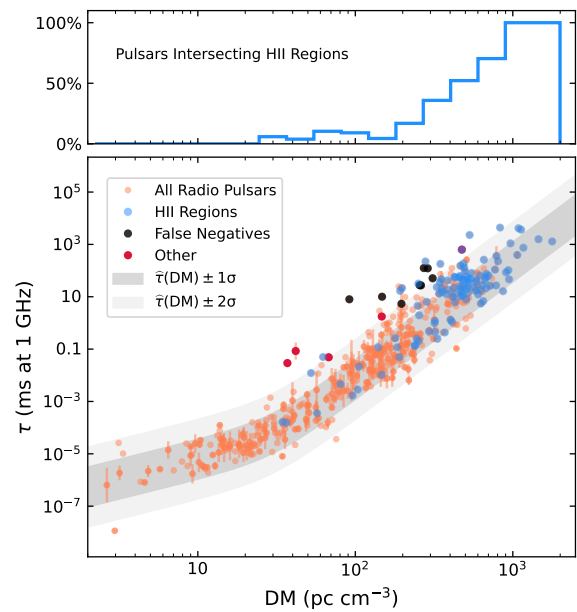


Figure 3. Pulse broadening time (τ) in ms at 1 GHz vs. DM for 500 pulsars (orange points) with scattering measurements compiled by this work and Cordes et al. (2016, 2022), where τ has been referenced to a frequency $\nu = 1$ GHz assuming $\tau \propto \nu^{-4}$. The grey and light grey bands show the 1σ (68%) and 2σ (95%) confidence intervals of the best-fit empirical τ -DM relation from Cordes et al. (2022). Blue points indicate pulsars identified as intersecting H II regions based on the criteria described in Section 3, and black points show false negatives, i.e., intersections that were missed due to the H II region lacking a distance measurement or due to a misestimated pulsar distance. We only searched for false negatives among pulsars with τ more than 2σ larger than the best-fit τ -DM relation. Red points indicate outliers with large scattering that intersect discrete structures other than H II regions; these include pulsars within supernova remnants and pulsars intersecting the Gum Nebula and the Orion-Eridanus superbubble. The top panel shows the fraction of pulsars that intersect H II regions, in individually normalized DM bins.

erties. Each pulsar-H II region pair was validated against multi-wavelength maps, and about 30 spurious intersections have been excluded from an initial sample of 134 candidates. Most of the spurious candidates correspond to H II regions in HH14 with small near kinematic distances, leading to an inaccurately large angular diameter used for the impact parameter cutoff. We thus estimate a false positive rate of $\approx 20\%$ for the full set of 660 intersections identified above. For some pulsars, our criteria yielded multiple H II region intersections; these cases are noted in Table A1 but we only report properties for the H II region closest to the pulsar LOS.

To estimate a false negative rate for our intersection analysis, we focus on a subset of pulsars with scattering in excess of values typical for a given DM. When the observed scattering times of many pulsars are referenced to a single observing frequency ν (assuming, e.g., $\tau \propto \nu^{-4}$; Rick-

ett 1990), they show a nonlinear, positive correlation with DM (Cordes et al. 1991; Bhat et al. 2004; Krishnakumar et al. 2015; Cordes et al. 2016). This empirical τ -DM relation has the form (Cordes et al. 2022): $\hat{\tau}(1 \text{ GHz}) = (1.9 \times 10^{-7} \text{ ms}) \text{DM}^{1.5}(1 + 3.55 \times 10^{-5} \text{DM}^3)$. Figure 3 shows the distribution of scattering times vs. DMs and the best-fit τ -DM relation, which has a 68% confidence interval $\sigma(\log_{10} \tau) = 0.76$ (Cordes et al. 2022). Twenty-six pulsars in our sample have τ more than 2σ greater than the τ -DM relation (hereafter referred to as “excess scattering”), with eight of these pulsars positively identified as intersecting H II regions. Out of the remaining 18 pulsars with excess scattering, 8 are spatially coincident in multi-wavelength maps with H II regions in the WISE and HH14 catalogs and appear to have been missed by the intersection analysis, due to a combination of the H II regions lacking distance measurements and misestimated pulsar distances. Another 5 of the pulsars with excess scattering intersect known structures that are not H II regions, including supernova remnants, the Gum Nebula, and the Orion-Eridanus superbubble, based on assessment of their locations, angular extents, and estimated distances. We are unable to identify known foreground structures for the 5 remaining pulsars with large scattering. The full list of pulsar scattering outliers and potentially relevant foreground structures is given in Appendix B; the appendix also include cases where τ is over 2σ smaller than the mean τ -DM relation, which may be attributable to discrete structures close enough to the source that they contribute a DM enhancement but no significant scattering relative to the ISM (Cordes et al. 2016).

We thus find that the majority of pulsars with excess scattering intersect a known discrete structure in the ISM, with more than half of those structures being H II regions. Based on the H II region intersections that were missed for these cases, we estimate the false negative rate to be between $\approx 8/500 = 2\%$ and $8/26 = 30\%$, where we regard the latter value as an upper limit because it is based on only those pulsars with excess scattering.

Given the impact parameter cutoff used to identify H II region intersections, it is likely that the false positive and negative rates estimated above correspond to H II regions around specific star types. Many of the false positive intersections may correspond to B-type stars and later, which are typically smaller than the 20 pc impact parameter cutoff assumed for the HH14 cross-match. Conversely, many of the missed intersections may correspond to early O-type stars, which can have sizes > 20 pc (Rubin 1968). Despite their small sizes, H II regions around B1/B2 stars (in addition to white dwarfs), may be sufficient in number to enhance the overall density of the warm ionized medium (WIM), particularly in the inner galaxy. We thus argue that the purity of the intersection sample is not critical to our subsequent analysis, because even the

false positive intersections provide a diagnostic of the extent to which H II regions can enhance the WIM.

4. GENERAL TRENDS

We find that the majority of pulsars with large DM and τ intersect H II regions. Figure 2 shows the fraction of pulsars intersecting H II regions as functions of both DM and Galactic longitude, for all radio pulsars at Galactic latitudes $|b| < 5^\circ$. Given that H II regions are largely confined to the Galactic plane, we are interested in comparing the radio properties of pulsars intersecting H II regions against the radio properties of other pulsars in the plane. For these low-latitude pulsars, we find that $> 50\%$ of pulsars with $\text{DM} > 580 \text{ pc cm}^{-3}$ are identified as intersecting H II regions. These intersections are roughly uniform across longitudes $|l| \lesssim 50^\circ$, with notable clusters of intersections around $l \approx 150^\circ$, $l \approx 80^\circ$, $l \approx -100^\circ$, and $l \approx -175^\circ$ (likely caused by several prominent H II regions, including S205, the Cygnus region, S273, S264, and a series of H II regions along the upper edge of the Gum Nebula). Figure 2 also shows the maximum DM predicted by NE2001 in the Galactic plane, demonstrating that most of the pulsars with $\text{DM} > \text{DM}_\infty(\text{NE2001})$ intersect H II regions. The maximum DM predicted by YMW16 is generally larger than that of NE2001, but we similarly find that most of the pulsars with $\text{DM} > \text{DM}_\infty(\text{YMW16})$ lie behind H II regions.

For the pulsars with scattering measurements, $> 50\%$ of pulsars with $\text{DM} > 600 \text{ pc cm}^{-3}$ and $\tau > 10 \text{ ms}$ at 1 GHz are identified as intersecting H II regions. The fraction of these pulsars behind H II regions is a steep function of DM that grows roughly as DM^3 , which would be expected for an intersection probability that scales with the volume probed. Previous studies have linked small samples of both pulsars and extragalactic radio sources with large scattering to H II region envelopes (Anantharamaiah & Narayan 1988) and regions of high H α emission (Spangler & Reynolds 1990), supporting interpretations of the τ -DM relation that attribute the steepening of the relation at high DM to enhanced density fluctuations in the inner Galaxy (Cordes et al. 1991; Ocker et al. 2021). Complementary assessments of Faraday rotation measures (RMs) have shown that RM variations in the Local and Carina spiral arms are consistent with a turbulence injection scale $\approx 2 \text{ pc}$ (Haverkorn et al. 2004), suggesting that H II regions play a role in the turbulence cascade that gives rise to pulsar scattering. Our results support this general picture, but H II regions do not appear to be solely responsible for the steepening of the τ -DM relation, as evidenced by the many pulsars between $100 \lesssim \text{DM} \lesssim 600 \text{ pc cm}^{-3}$ that are not in the H II region sample (see Figure 3). However, some of these moderate-DM pulsars are likely missed intersections, in part because there are many more H II regions with inferred distances in the inner Galaxy.

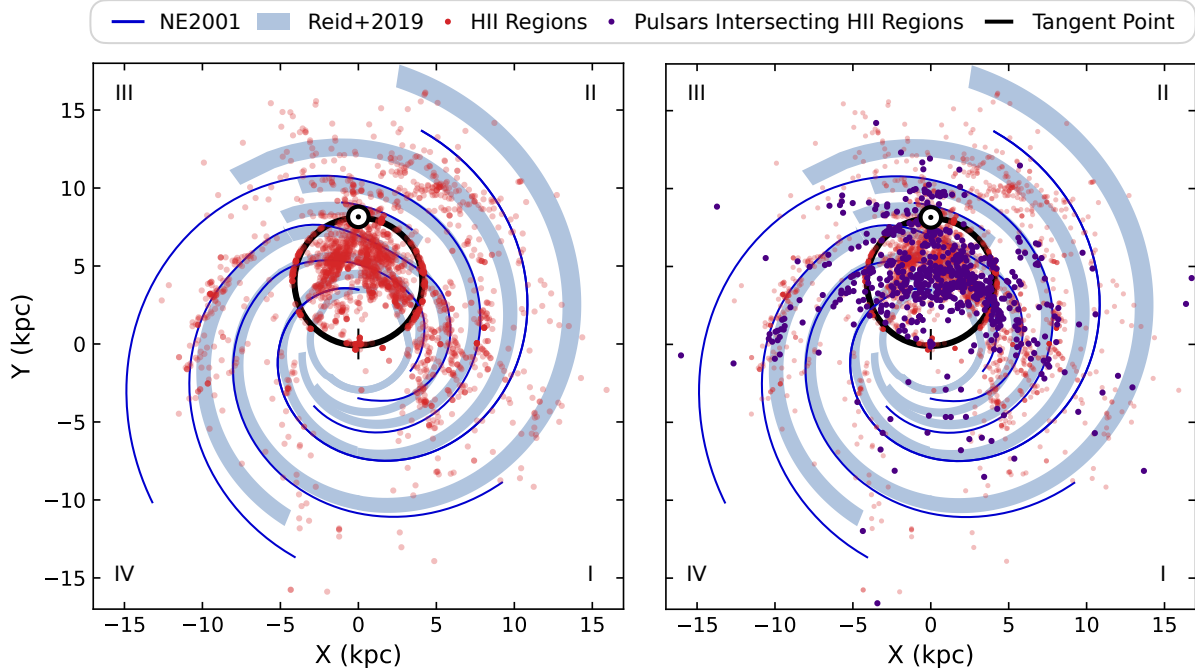


Figure 4. Distribution of H II regions and pulsar intersections projected onto the Galactic plane, with the Galactic Center at the origin. *Left:* H II regions with cataloged distances (red points) are superposed on the spiral arm model used in NE2001 (blue curves) and the Reid et al. (2019) best-fit model (light blue shaded curves). Tangent point distances lie along the black circle. Galactic quadrant numbers are noted in the corners. *Right:* Pulsars identified as intersecting H II regions are shown in purple. Most of the pulsar distances shown here are estimated using Galactic electron density models. We thus expect that many of these pulsars, including those near the outskirts of the Galaxy, are closer to the observer than they appear in this figure.

Figure 4 shows the locations of H II regions with distances in the WISE and HH14 catalogs, along with the pulsar intersections identified in Section 3.2, projected onto the Galactic plane. Several selection effects are evident in this figure, and demonstrate the sources of observational bias inherent in our results. First, there are many more H II regions with inferred distances in the inner Galaxy of quadrant I. This asymmetry in the distribution of H II region distances is partially due to radio telescope coverage at higher sensitivity, leading to a more complete distribution of radial velocities and distances in quadrant I (Anderson et al. 2012). A similar asymmetry manifests in the distribution of pulsars because of the northern PALFA pulsar survey (Cordes et al. 2006; Parent et al. 2022). Uncertainties in the H II region distances are complex, depending on the inference method used and the H II region location. Kinematic distances in the inner Galaxy are highly uncertain when they correspond to radial velocities near the maximum velocity of the inner Galaxy. These tangent point distances are highlighted in Figure 4 and appear as a circular artifact when projected onto the Galactic plane. The most precise distances for H II regions are based on maser parallaxes and are almost exclusively in quadrants I and II (Reid et al. 2019). Taken together, these various selection effects suggest that false positive intersections in our analysis are predominantly for LOSs in the inner Galaxy, where

kinematic distance uncertainties are large, and that more intersections are missed (false negatives) in quadrants III and IV, where the sample of H II region distances is less complete. Figure 4 also shows spiral arm models from NE2001 and Reid et al. (2019); these models are discussed further in Section 7.

5. COMPARISON TO RADIO RECOMBINATION LINES

Having found that the majority of pulsars with large DM and τ lie behind H II regions, we now must ask: How much of their DM and scattering is contributed by the H II regions vs. the rest of the ISM along the LOS? Recombination lines provide an independent observational constraint on the electron density content of these regions via estimation of their emission measures ($EM = \int n_e^2 dl$). Many of the H II regions in our sample do not have optical recombination line observations at the spatial resolution needed for even a broad comparison to pulsars in our sample. We hence turn to radio surveys of H II regions, which have the added benefit of not suffering from dust extinction. We select three areas on the sky that contain a few dozen pulsars behind H II regions, and that have been covered by radio surveys with sufficient sensitivity and resolution to estimate EMs near the pulsar LOSs for comparison to DM and scattering. These three sky areas are shown in Figure 5, using data from subsets of three

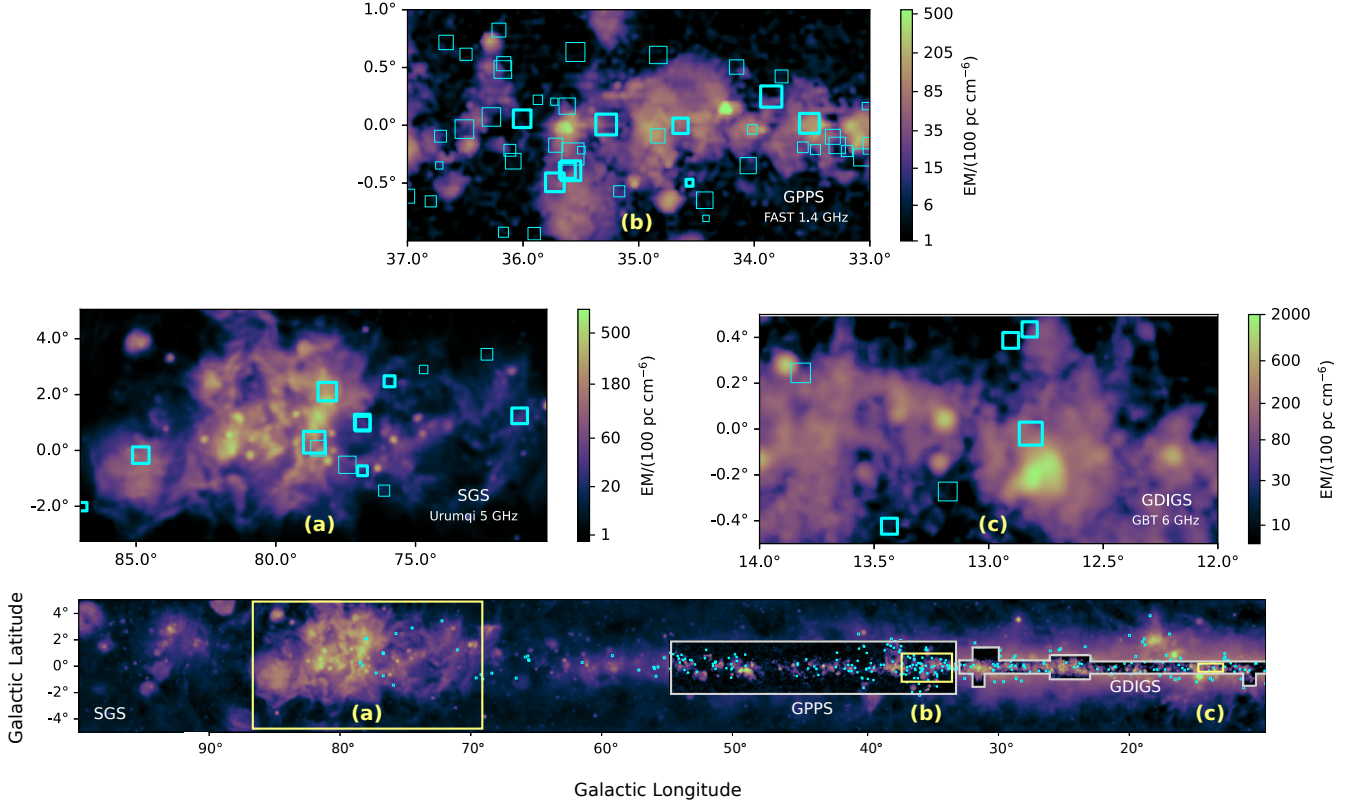


Figure 5. Maps of emission measure (EM) in units of 100 pc cm^{-6} for three sky areas containing H II regions along pulsar LOSs (cyan squares). The bottom panel demonstrates the regions selected from each survey for comparing H II region EMs to pulsar DMs (yellow squares). GDIGS and SGS respectively extend to smaller and larger longitudes than shown here. Panel (a) shows EM estimated from total intensity measured by SGS (Sun et al. 2007) at Urumqi, assuming an RRL-to-continuum ratio of 13% and a 25 km s^{-1} line width (§5.1). Panels (b) and (c) show EM estimated from H α intensity maps measured by the GPPS (Hou et al. 2022) and GDIGS (Anderson et al. 2021) surveys. The sizes of the cyan squares indicate the relative magnitudes of the pulsars’ DMs (larger squares mean larger DMs). Thicker squares are pulsars with scattering measurements.

radio surveys: the Green Bank Diffuse Ionized Gas Survey (GDIGS; Anderson et al. 2021), FAST GPPS (Hou et al. 2022), and the Sino-German 6 cm Survey (SGS) (Sun et al. 2007, 2011; Xiao et al. 2011; Gao et al. 2019). Table 1 gives an overview of the three surveys. While the total sky coverage of the surveys includes nearly half of the Galactic plane, we focus on the three areas shown in Figure 5 because they each contain multiple pulsars where the H II regions’ radio emission is bright enough to accurately infer EMs.

5.1. Emission Measure Maps

GDIGS and FAST GPPS both have the spectral resolution needed to distinguish the H α recombination line transition (in addition to H $n\beta$ and H $n\gamma$) and they provide velocity-integrated H α intensity maps in their respective frequency ranges. In local thermodynamic equilibrium, the velocity-integrated line intensity W_{RRL} is related to EM as (Gordon

& Sorochenko 2002; Anderson et al. 2021):

$$\frac{\text{EM}}{\text{pc cm}^{-6}} \approx 1150 \left(\frac{\nu}{\text{GHz}} \right) \left(\frac{T_e}{8000 \text{ K}} \right)^{3/2} \left(\frac{W_{\text{RRL}}}{\text{K km s}^{-1}} \right), \quad (1)$$

where T_e is the electron temperature and ν is the frequency of the line transition. The pre-factor in Equation 1 applies only to H α lines (i.e., an energy level transition $\Delta n = 1$; see Appendix A of Anderson et al. 2021). H II regions typically have $T_e \approx 8000 \text{ K}$, although inferred values can range from $\approx 5,000 - 20,000 \text{ K}$ (equivalent to up to a factor of 4 change in estimated EM) and tend to increase with Galactocentric radius (Quireza et al. 2006b). We use the best-fit form of T_e as a function of Galactocentric radius R_{gal} from Quireza et al. (2006b),

$$T_e = (5780 \pm 350) + (287 \pm 46) R_{\text{gal}} \quad (2)$$

and we estimate T_e for H II regions in each of the sky areas we examine. To estimate the resulting EM and its uncertainty, we sample from normal probability density functions (PDFs) for both T_e and the RRL intensity W_{RRL} , based on

Table 1. Radio Surveys of H II Regions

Survey	Telescope	Observing Frequency	Sky Coverage	Angular Resolution	Median W_{RRL} Uncertainty	EM Sensitivity
GDIGS	GBT	4–8 GHz	$32.3^\circ > l > -5^\circ, b < 0.5^\circ$	2.65'	0.26 K km/s	1100 pc cm ⁻⁶
GPPS	FAST	1–1.5 GHz	$55^\circ > l > 33^\circ, b < 2^\circ$	3'	0.16 K km/s	200 pc cm ⁻⁶
SGS	Urumqi	4.5–5.1 GHz	$10^\circ < l < 230^\circ, b < 5^\circ$	9'.5	–	–

NOTE—Overview of the three radio surveys used in this work: the Green Bank Diffuse Ionized Gas Survey (GDIGS; Anderson et al. 2021), the FAST Galactic Plane Pulsar Survey (GPPS; Hou et al. 2022), and the Sino-German 6 cm Survey (SGS; Gao et al. 2019). The sky coverages shown correspond to the total survey footprints, of which we only use a portion in our analysis. The rightmost two columns give the median uncertainty in RRL line intensity assuming a 25 km/s line width, and an equivalent EM sensitivity for $T_e = 8000$ K and a 3σ detection threshold. Both GDIGS and GPPS resolve RRLs (Hn α , Hn β , Hn γ) and provide maps of Hn α integrated intensity. SGS does not resolve RRLs but has a total brightness temperature sensitivity of ≈ 1 mK, comparable to the sensitivity of GDIGS when integrating over all Hn α lines.

the 68% confidence intervals of the T_e gradient and the rms spectral noise of the RRL intensity maps, respectively.

SGS does not provide velocity-integrated Hn α maps, and so we convert from total intensity to EM by assuming an Hn α line width of 25 km s⁻¹ and a line-to-continuum ratio (R_{LC} ; the ratio of RRL intensity to the total radio intensity integrated over the total frequency bandwidth). SGS is one of the most sensitive radio surveys with contiguous coverage of Galactic longitudes $90^\circ > l > 70^\circ$, which is a region of high interest because it contains a large (≈ 90 deg²) complex of H II regions and the pulsars identified both by Han et al. (2021) and this work as having DMs significantly greater than Galactic model predictions. This sky area (which includes the famous Cygnus region) has only been partially covered by previous RRL surveys, including GDIGS and Barcia et al. (1985), Heiles et al. (1996), and Azcárate et al. (1997). We leverage GDIGS Hn α maps covering a portion of Cygnus to estimate R_{LC} , finding it to be as low as 4% in the faintest regions and as high as 30% in the brightest, with the majority of locations in the range of 10–15%. These ratios are entirely consistent with empirical ratios for dozens of other H II regions (Quireza et al. 2006a). We therefore adopt a mean value $R_{\text{LC}} = 13\%$, and for subsequent analysis we adopt a log-normal PDF for R_{LC} spanning the range of values given above.

Figure 5 shows maps of the EMs inferred from subsets of these three surveys using Equation 1, based on the measured line intensities and median value of T_e in each sky area. The smallest EMs inferred are comparable to the sensitivities listed in Table 1, but are dramatically larger ($> 10^4$ pc cm⁻⁶) near the centers of the H II regions. Table 1 gives the median W_{RRL} uncertainty for each survey, which combined with uncertainties in T_e (due to both scatter in the T_e gradient and uncertainty in the H II region distances) yields typical EM uncertainties $\approx 30 - 60\%$. The spectral noise in all of these survey maps varies spatially by up to $\approx 200\%$, with the highest noise levels corresponding to regions of highest radio intensity. For SGS, we do not have velocity-resolved spectral rms measurements. However, the total brightness tem-

perature sensitivity reported for SGS by Xiao et al. (2011), 1 mK, is very similar to the brightness temperature sensitivity of GDIGS after integrating over all Hn α lines (Anderson et al. 2021). We consequently assume that the equivalent W_{RRL} uncertainty is similar, and add it in quadrature to the uncertainty associated with R_{LC} .

5.2. Relating Emission Measure to Dispersion Measure

We relate EM to DM using an ionized cloudlet model, in which cloudlets have a local volume-averaged mean density n_e and internal density $n_{e,i}$, such that $n_e = f n_{e,i}$ for a volume filling factor f . The electron density fluctuation variance within a cloudlet is $\epsilon^2 = (\langle (\delta n_{e,i})^2 \rangle) / n_{e,i}^2$, and variations between cloudlets $\zeta = \langle n_{e,i}^2 \rangle / \langle n_{e,i} \rangle^2$ (Cordes et al. 1991; Taylor & Cordes 1993; Cordes & Lazio 2002). Figure 6 shows a schematic of the model. The resulting relation between EM and DM is

$$\text{EM} = \frac{\zeta(1 + \epsilon^2)}{fL} \text{DM}^2, \quad (3)$$

where L is the path length through the relevant volume of cloudlets—in our case, the path length through an H II region (see also Appendix B of Cordes et al. 2016). Here ζ , ϵ , and f are dimensionless quantities, and L and DM have their usual units of pc and pc cm⁻³. In practice, $\zeta \geq 1$, $\epsilon^2 \leq 1$, and $f \leq 1$, and we can place an upper limit on DM for a given EM, f , and L by assuming $\zeta \rightarrow 1$ and $\epsilon^2 \rightarrow 0$ (corresponding to the limit of no turbulent fluctuations within cloudlets):

$$\text{DM} \leq 100 \text{ pc cm}^{-3} \times (f_{0.1} L_{10} \text{EM}_4)^{1/2} \quad (4)$$

where $f_{0.1} = f/0.1$, $L_{10} = L/(10 \text{ pc})$, and $\text{EM}_4 = \text{EM}/(10^4 \text{ pc cm}^{-6})$. The equivalent volume-averaged mean electron density would be $n_e = \text{DM}/L$, or

$$n_e \leq 10 \text{ cm}^{-3} (f_{0.1} \text{EM}_4 / L_{10})^{1/2}. \quad (5)$$

Figure 7 shows the distribution of EM vs. DM for the pulsars covered by each cutout of GDIGS, GPPS, and SGS. The EM is estimated for each pulsar LOS using the nearest map

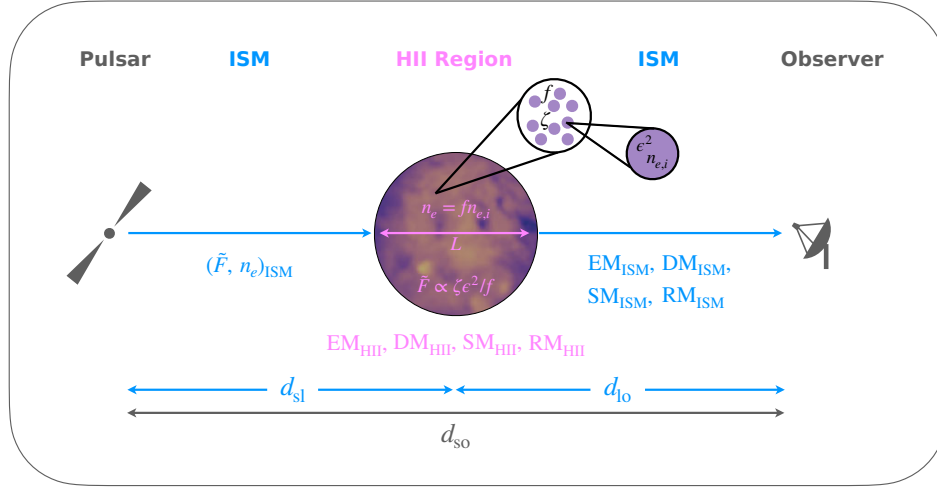


Figure 6. Schematic of the ionized cloudlet model used to relate pulsar and emission line observables (§5.2-6). H II regions are modeled with electron densities n_e and density fluctuation parameters \tilde{F} . The fluctuation parameter depends on the interior properties of the H II region, described by the volume filling factor of cloudlets f , the density variance within cloudlets ϵ^2 , and density variations between cloudlets ζ . The ISM is described by separate n_e and \tilde{F} . The relevant observables are emission measure (EM), dispersion measure (DM), scattering measure (SM, which is related to the scattering delay τ), and rotation measure (RM). In this work we only consider relations between EM, DM, and τ .

pixel and evaluating T_e for the Galactocentric radius of the intersected H II region (Equation 2). There is only weak correlation (Pearson’s coefficient $r = 0.4$) between EM and total observed DM, which is unsurprising given that the total DMs include contributions from ionized gas in the diffuse ISM, and given that variations in f , L , ζ , and ϵ between different regions are guaranteed. Estimating the DM contribution from the diffuse ISM alone is fraught in the absence of distance measurements for these pulsars, which would enable rough tomography of these sky regions. We instead focus on estimating the range of possible DMs that could be contributed by the H II regions (DM_{HII}) based on their EMs. Figure 7 shows the maximum DM estimated from EM based on Equation 4 for the pulsars in the GDIGS, GPPS, and SGS fields, assuming $f = 0.1$ and $L = 10$ pc, which are considered typical for 10^4 K ionized gas and H II regions (Draine 2011). The resulting upper limits on DM_{HII} range from ≈ 15 to 200 pc cm^{-3} , with median values $\approx 10\%$ of the total observed DM.

These fiducial EM-inferred DMs may underestimate the DM contributions of the H II regions, particularly for those pulsars which have total DMs greater than Galactic models’ maximum predictions. For example, PSR J2030+3944g has a DM excess of 540 pc cm^{-3} greater than DM_{∞} predicted by NE2001, but the fiducial value $\text{DM}_{\text{HII}}^{\text{max}}(f = 0.1, L = 10) \approx 180 \text{ pc cm}^{-3}$ suggests that f and/or L must be larger for the H II region to account for the pulsar’s excess DM.

We examine this further by estimating PDFs for DM_{HII} through a likelihood analysis of each pulsar with a total DM

in excess of DM_{∞} (NE2001). The per-pulsar PDF is

$$p(\text{DM}_{\text{HII}}|\text{EM}, F_{\ell}) \sim \int d\text{EM} dF_{\ell} p(\text{EM})p(F_{\ell}) \times \delta[\text{DM}_{\text{HII}} - \mathcal{G}(\text{EM}, F_{\ell})], \quad (6)$$

where $F_{\ell} = fL/\zeta(1 + \epsilon^2)$ and $\mathcal{G}(\text{EM}, F_{\ell})$ is the function relating DM and EM (Equation 3). The PDF for EM is evaluated using priors on T_e , W_{RRL} , and R_{LC} described in Section 5.1, and we adopt a flat prior for F_{ℓ} restricted to the range $[0.1, 50]$ pc, which includes cases spanning $f/\zeta(1 + \epsilon^2) \ll 1$ to $f/\zeta(1 + \epsilon^2) \sim 1$ and $L \sim 5$ to 50 pc. We then compare $p(\text{DM}_{\text{HII}})$ to $\text{DM}_{\text{excess}} = \text{DM}_{\text{tot}} - \text{DM}_{\infty}$ (NE2001), the pulsar’s excess from the maximum Galactic DM prediction for that LOS, and use a numerical joint likelihood analysis of $p(\text{DM}_{\text{HII}})$ and $\text{DM}_{\text{excess}}$ to yield a posterior PDF for F_{ℓ} . In short, we search for the range of F_{ℓ} that allows the H II region’s EMs to account for each pulsar’s entire excess DM.

Figure 8 shows an example of $p(\text{DM}_{\text{HII}})$ for PSR J2030+3944g, which has the largest excess DM in our sample, compared to the value of DM_{HII} that would be inferred assuming $F_{\ell} = 1$ pc, which is equivalent to the upper limit $\text{DM}_{\text{HII}}^{\text{max}}$ for $f = 0.1$, $L = 10$ pc, and $\zeta = 1 + \epsilon^2 = 1$. In order for the H II region’s EM to account for the entire excess DM, F_{ℓ} must be larger, and we find $F_{\ell} = 13_{-4}^{+5}$ pc (corresponding to the $50\%_{-35\%}^{+35\%}$ confidence intervals of the posterior PDF). We perform this analysis for all of the pulsars covered by the EM maps in Figure 5 with DMs in excess of the predicted maximum DM, which yields constraints on F_{ℓ} for six LOSs shown in Table 2. Half of these pulsars have $F_{\ell} \sim 1$ to 5 pc, broadly consistent with standard assumptions of f and L for the case $\zeta = 1 + \epsilon^2 = 1$. In one

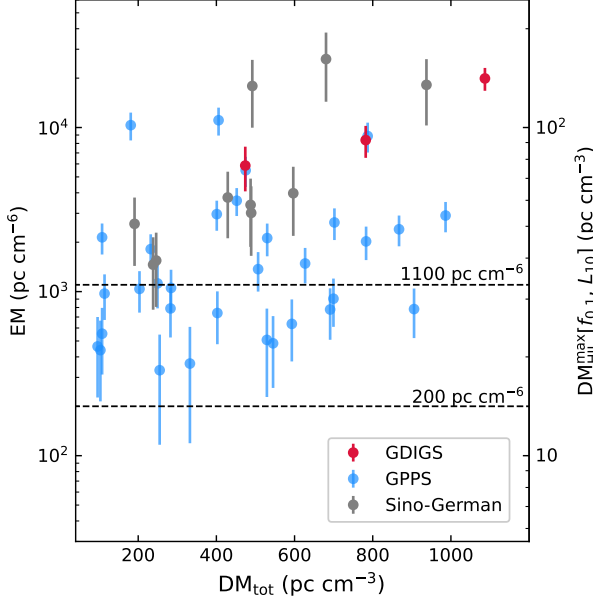


Figure 7. EM vs. total observed DM for pulsars in the three sky regions shown in Figure 5. Pulsars covered by a portion of the GDIGS survey are shown in red, those covered by a portion of GPPS in blue, and those covered by a portion of SGS in grey. EMs were calculated using the procedure given in Sections 5.1-5.2. Error bars account for the uncertainties of both W_{RRL} (Table 1) and T_e (Section 5.1). For the SGS data we assume the same median W_{RRL} uncertainty as for GDIGS, and we sample from a log-normal PDF for R_{LC} to include its uncertainties in the error bars shown. Pulsar LOSs with EMs smaller than the survey’s EM sensitivity and fractional EM errors $> 75\%$ have been excluded. The right-hand axis shows the equivalent upper limit on DM assuming a volume filling factor $f = 0.1$ and a path length through the H II region $L = 10$ pc (see Section 5.2).

case, J2030+3929g, $F_\ell < 1$ and the EM is similar in value to the pulsars with $\text{DM}_{\text{excess}} > 300 \text{ pc cm}^{-3}$, which suggests that the H II region may account for even more of the pulsar’s DM. In principle, these constraints on F_ℓ are lower limits because $\text{DM}_\infty(\text{NE2001})$ provides an upper bound on the ISM contribution to DM along the pulsar LOS, and hence $\text{DM}_{\text{excess}}$ (and F_ℓ) could be even larger.

Our results suggest that for naive assumptions about f and L , the EMs inferred from RRL surveys can easily produce DM contributions $\sim 10\text{--}10^2 \text{ pc cm}^{-3}$ from H II regions. Allowing for an agnostic range of f , L , ζ , and ϵ can increase the DM contributions of these H II regions to several hundreds of pc cm^{-3} , which explains those pulsars with DMs far greater than the maximum model predictions for their LOSs.

All of the pulsars shown in Table 2 are in the vicinity of the Cygnus OB1 association. Previous assessments of extragalactic radio sources have found that Cygnus is a source of substantial scattering (Spangler & Cordes 1998) and variations in Faraday RMs as large as $\sim 100\text{s}$ of rad m^{-2} (Lazio

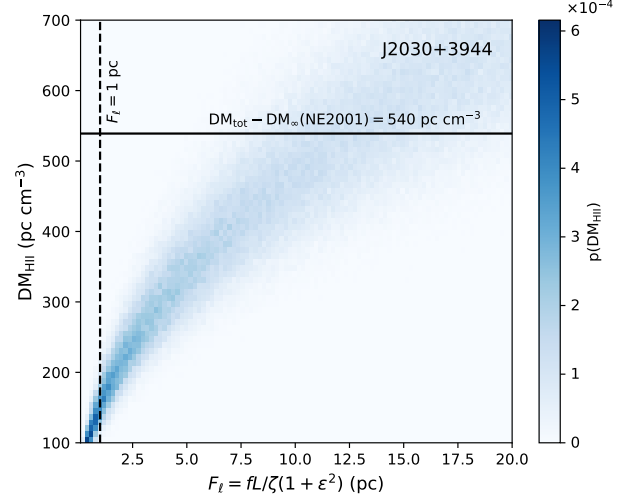


Figure 8. Probability density for DM_{HII} vs. F_ℓ for PSR J2030+3944g, calculated via the likelihood analysis described in Section 5.2, which assumes a flat prior on F_ℓ . The black horizontal line indicates the pulsar’s excess DM from NE2001’s maximum DM for that LOS, and the vertical dashed line indicates the fiducial value $F_\ell = 1$, which would yield the upper limit $\text{DM}_{\text{HII}}^{\text{max}}$ for $f = 0.1$, $L = 10$ pc, and $\zeta = 1 + \epsilon^2 = 1$, as assumed in Figure 7. In order for the H II region’s EM to be consistent with the entire excess DM, the PDF for DM_{HII} requires $F_\ell = 13^{+5}_{-4}$ pc. This constraint on F_ℓ is a lower limit because $\text{DM}_\infty(\text{NE2001})$ can be considered an upper bound on the ISM contribution to the pulsar’s DM.

Table 2. Constraints on F_ℓ for Pulsars with $\text{DM}_{\text{tot}} > \text{DM}_\infty(\text{NE2001})$

PSR	$\text{DM}_{\text{excess}}$ (pc cm^{-3})	EM (10^3 pc cm^{-6})	F_ℓ (pc)
J2005+3411g	73	$3.6^{+1.4}_{-1.0}$	$1.5^{+0.5}_{-0.4}$
J2030+3929g	91	$21.1^{+8.6}_{-5.9}$	$0.4^{+0.1}_{-0.1}$
J2022+3845g	94	$3.9^{+1.5}_{-1.0}$	$2.3^{+0.9}_{-0.6}$
J2030+3818g	194	$4.5^{+1.6}_{-1.2}$	$8.5^{+3.1}_{-2.3}$
J2021+4024g	331	$32.2^{+11.1}_{-8.6}$	$3.4^{+1.2}_{-0.9}$
J2030+3944g	540	$21.8^{+8.1}_{-5.9}$	13^{+5}_{-4}

NOTE—Values shown for F_ℓ correspond to lower limits based on the requirement that the H II region EM be consistent with the entire DM excess from $\text{DM}_\infty(\text{NE2001})$. Error bars correspond to the 15% and 85% confidence intervals, and include uncertainties in W_{RRL} , T_e , and R_{LC} .

et al. 1990; Whiting et al. 2009). While NE2001 includes about 10 clumps that reproduce the large scattering inferred from these prior studies, our assessment demonstrates that the DM contribution of Cygnus is up to $\sim 100\times$ larger than the model’s clump parameters ($\approx 10\text{--}40 \text{ pc cm}^{-3}$; Cordes & Lazio 2002), and a revised treatment of Cygnus will be needed in a next-generation Galactic electron density model.

6. SCATTERING AND DENSITY FLUCTUATIONS

We use radio scattering measurements to constrain the density fluctuation properties of H II regions through an extension of the ionized cloudlet model introduced in Section 5. We initially assume that the H II regions are the dominant source of the pulsars' observed scattering (as supported by numerous studies that find radio wave scattering consistent with arising from H II regions; e.g., Spangler & Cordes 1998; Rickett et al. 2009; Mall et al. 2022; Ocker et al. 2024). Potential complications from this assumption are discussed at the end of this section.

6.1. Extension of the Ionized Cloudlet Model

The ionized cloudlet model introduced in Section 5.2 can be applied to the phenomenon of radio wave scattering by assuming a power spectrum of density fluctuations that extends down to spatial scales smaller than the Fresnel scale ($r_F \sim \sqrt{\lambda D} \sim 0.01$ au for typical distances D and observing wavelengths λ). Here we are primarily interested in the interpretation of the pulse broadening measurements shown in Figure 3, which characterize the frequency-dependent broadening of radio pulses in time due to multipath propagation. For a statistically homogeneous medium and a Kolmogorov spectrum of density fluctuations of the form $P_{\delta n_e} = C_n^2 q^{-11/3} \exp(-(ql_i/2\pi)^2)$, the pulse broadening time in Euclidean space is (Cordes et al. 2016; Ocker et al. 2021; Cordes et al. 2022):

$$\tau(\text{DM}, \nu) \approx 48.03 \text{ ns } A_\tau \nu_{\text{GHz}}^{-4} \tilde{F} G_{\text{scatt}} \text{DM}^2. \quad (7)$$

The prefactor given in Equation 7 for $\tau(\text{DM}, \nu)$ is evaluated for ν in GHz and DM in pc cm^{-3} . The dimensionless factor $A_\tau \leq 1$ converts the mean pulse broadening time to the $1/e$ time that is typically estimated from pulse shapes. The exact value of A_τ depends on unknown properties of the scattering medium, and we proceed by assuming $A_\tau = 1$, which corresponds to the exponential scattering tail of a Gaussian scattered image.

The density fluctuation spectrum introduced above depends on C_n^2 , the spectral amplitude, and $q = 2\pi/l$, the wavenumber for fluctuations at a given spatial scale l , where the spectrum extends from $2\pi/l_o \lesssim q \lesssim 2\pi/l_i$ for outer and inner scales l_o, l_i . For an H II region, the outer scale is likely similar to the scale of the ionizing star's interaction with the ISM (comparable to the Strömgren sphere radius, ~ 10 s of pc for O-type stars). The inner scale will be orders of magnitude smaller. In one case, Rickett et al. (2009) measured the pulse broadening shape of the pulsar J1644–4559, which lies behind H II region G339.1–0.4 (see Appendix A), at high enough precision to distinguish between different turbulence models, and found $l_i \approx 70 - 100$ km. The values of l_o and l_i likely vary between H II regions, so we combine these and the other unknown quantities describing the density

fluctuation statistics of the medium into a composite density fluctuation parameter given by

$$\tilde{F} \approx 0.08 (\text{pc}^2 \text{km})^{-1/3} \frac{\zeta \epsilon^2}{f} \times \left(\frac{l_o}{20 \text{ pc}} \right)^{-2/3} \left(\frac{l_i}{100 \text{ km}} \right)^{-1/3}. \quad (8)$$

The geometric leverage factor G_{scatt} is derived from the standard Euclidean weighting of C_n^2 and is given by (see Cordes et al. 2022):

$$G_{\text{scatt}}(x, y) = \frac{1 - (2x/3) + (2y/x)(1 - y - x)}{1 - (2x/3)} \quad (9)$$

where $x = L/d_{\text{so}}$ and $y = d_{\text{sl}}/d_{\text{so}}$ for a scattering layer of thickness L at a distance d_{sl} from the source and a source-to-observer distance d_{so} .

The empirical τ -DM relation observed for Galactic pulsars (Figure 3) can be interpreted through this model as the result of variations in both \tilde{F} and G_{scatt} : LOSs towards the inner Galaxy have systematically higher \tilde{F} , leading to a different slope of the τ -DM relation at high DMs, and LOSs at a given DM have different G_{scatt} , leading to broad spread in τ for a fixed DM (Cordes et al. 2022). If we simplistically assume that all pulsars are embedded in their scattering media (i.e., scattering is dominated by the extended ISM), then $G_{\text{scatt}} \approx 1/3$ and the resulting distribution of \tilde{F} varies by over 5 orders of magnitude between the inner and outer Galaxy, and as a function of Galactic latitude (Ocker et al. 2021). Conversely, if scattering is dominated by discrete structures, then $G_{\text{scatt}} > 1$ and we must explicitly account for how those structures are distributed along pulsar LOSs.

6.2. The Density Fluctuation Parameter in H II Regions

In practice, G_{scatt} and \tilde{F} are only constrained when the distances of both the pulsar and scattering layer are known. There are five pulsars in our sample of scattering measurements that have precise parallax distances, J0357+5236, J0358+5413, J0601–0527, J1614–2230, and J1643–1224. The first two lie towards the Galactic anticenter and the latter three lie at Galactic latitudes $|b| > 10^\circ$. We estimate the DM contributions of the H II regions along these LOSs by assuming the best-fit plane-parallel model for the electron density structure of the thick disk, which has a mid-plane density of $n_0 = 0.015 \pm 0.001 \text{ cm}^{-3}$ and a scale height of 1.57 ± 0.15 kpc (Ocker et al. 2020). While this model is most accurate for high Galactic latitudes, it appears to give reasonable estimates for the two pulsars in the plane, J0357+5236 and J0358+5413, for reasons discussed below.

The DM contributions of the ISM and H II regions for these pulsars, based on the Ocker et al. (2020) plane-parallel model, are shown in Table 3, along with resulting estimates

of $\tilde{F}G_{\text{scatt}}$ that assume the observed scattering is dominated by the H II region. Pulsars J0357+5236 and J0358+5413 lie in the plane at Galactic longitudes $l \approx 149^\circ$, and both intersect the H II region S205 (Mitra et al. 2003). The smooth plane-parallel model tends to be inaccurate at low Galactic latitudes, due primarily to the presence of spiral arms and increased density variance associated with discrete structures. In this case, the source of the density variance is known, and assuming the mid-plane density of 0.015 cm^{-3} yields DM contributions from the H II region that are very similar for both pulsars, and comparable to the H II region DMs estimated for the pulsars at higher latitudes.

The density fluctuation parameter \tilde{F} is estimated by assuming normal PDFs for the pulsar parallaxes, H II region distances, DMs, and τ . A uniform PDF is evaluated for L that is based on the path length through a sphere with radius given by the angular diameter of the H II region and its distance, along with the pulsar’s transverse distance from the center of the H II region. The PDF width for L is determined by the uncertainty in the H II region distance, except in the case of J0601–0527 where the H II region distance is a lower limit and we instead evaluate the PDF for the minimum physical diameter that allows the pulsar LOS to have a non-zero path length through the H II region. Assuming that all of the observed scattering is attributable to the H II regions yields the estimates of \tilde{F} shown in Table 3, which can be converted for an assumed inner scale to $\tilde{F}l_i^{1/3} \equiv F_c$, the fluctuation parameter that is conventionally used to estimate scattering measures.

We find \tilde{F} ranges from $\sim 10^{-4} - 10^{-2} (\text{pc}^2 \text{ km})^{-1/3}$, with the largest value corresponding to J1643–1224. This larger value is comparable to expectations for $l_o \sim 20 \text{ pc}$ and $l_i \sim 100 \text{ km}$, for $\zeta \approx \epsilon^2 \approx f \sim 1$. Leaving l_o , l_i , ζ , and f at the same nominal values as in Equation 8 would require $\epsilon \ll 1$ to explain the small values of \tilde{F} found for the other H II regions in Table 3. This statement is agnostic to changes in ζ and f because $f \leq 1$ and $\zeta \geq 1$.

The DM and scattering contributions of H II regions S7 and S27 were previously assessed for J1614–2230 and J1643–1224 by Ocker et al. (2020). Here we use an updated parallax distance for J1643–1224 from Ding et al. (2023), and unlike Ocker et al. (2020) we do not subtract an estimate of the ISM contribution to τ , nor do we assume the H II region diameter is equivalent to the path length through the region. These differences yield values of F_c that are smaller than those reported by Ocker et al. (2020) for these two pulsars.

The fluctuation parameters shown in Table 3 are smaller than values that would be inferred if we instead assumed that the pulsar scattering occurs in the extended ISM (in which case $G_{\text{scatt}} = 1/3$). We have also assumed that the pulsar’s entire path length through the H II region contributes to the

observed scattering. If the scattering is confined instead to the H II region boundary, or to an overdensity inside the H II region, then \tilde{F} will tend to be larger; e.g., re-evaluating the scattering time of J1643–1224 for a screen width $L \sim 1 \text{ pc}$ and a DM contribution $\sim 1 \text{ pc cm}^{-3}$ yields $G_{\text{scatt}} \approx 300$ and $\tilde{F} \sim 4 (\text{pc}^2 \text{ km})^{-1/3}$. While these degeneracies between screen width, DM, and \tilde{F} make it difficult to further interpret the values of \tilde{F} shown in Table 3, we can nonetheless assess the degree to which variations in DM, G_{scatt} , or \tilde{F} dominate the extreme differences in τ between nearby pulsars intersecting H II regions (such as those with parallax distances), and more distant pulsars intersecting H II regions, which show the largest measured scattering.

We focus on comparing two extremes in the distribution of τ for pulsars intersecting H II regions, illustrated in Figure 9: $\tau \sim 10^{-4} \text{ ms}$ and $\tau \sim 10^2 \text{ ms}$ at 1 GHz. In the low- τ case, we have found fiducial values of $\tilde{F} \sim 10^{-4} - 10^{-2} (\text{pc}^2 \text{ km})^{-1/3}$. Assuming these values of \tilde{F} apply to the high- τ case yields $\text{DM}^2 \times G_{\text{scatt}} \sim 10^8 - 10^{10} \text{ pc cm}^{-3}$. Such high values of $\text{DM}^2 \times G_{\text{scatt}}$ would require $L < 1 \text{ pc}$ and $\text{DM} > 10^3 \text{ pc cm}^{-3}$, corresponding not only to implausibly high electron densities but also DMs larger than typically observed. The two extremes in τ could conversely be reconciled for reasonable values of $\text{DM}^2 \times G_{\text{scatt}}$ if \tilde{F} is much larger ($\sim 1 - 100 (\text{pc}^2 \text{ km})^{-1/3}$) for the high- τ LOSs.

If the scattering of these pulsars is dominated by their foreground H II regions, then we are left with two possible conclusions: either the distribution of \tilde{F} for H II regions varies dramatically (perhaps due to underlying properties of the H II regions, such as age), or \tilde{F} is roughly the same for all H II regions and it is variations in $\text{DM}^2 \times G_{\text{scatt}}$ that lead to the large range in τ . We consider the latter conclusion less likely because large values of $\text{DM}^2 \times G_{\text{scatt}}$ would require that H II regions contribute $\text{DM} > 10^3 \text{ pc cm}^{-3}$, which combined with the ISM would imply DMs greater than observed. A larger sample of pulsars with $\text{DM} > 100 \text{ pc cm}^{-3}$ and known distances could be used to search for correlations between inferred estimates of \tilde{F} and other H II region properties, which may reveal whether variations in \tilde{F} between different H II regions can be plausibly linked to other tracers of their internal properties.

A complementary test of radio scattering by H II regions is through Fourier analysis of pulsar scintillation (i.e., scintillation arcs; Stinebring et al. 2001), which constrains the locations of scattering material and disentangles scattering from multiple locations along the LOS. Two of the pulsars in our sample, J0358+5236 and J1643–1224, have scintillation arcs that are consistent with scattering locations in their foreground H II regions, affirming that the H II regions contribute to the observed scattering (Mall et al. 2022; Ocker et al. 2024). However, in both of these cases, multiple arcs are detected at varying distances from the observer: for

Table 3. H II Region Density Fluctuation Parameter for Pulsars with Parallax Distances

PSR	τ (ms at 1 GHz)	DM _{ISM} (pc cm ⁻³)	DM _{HII} (pc cm ⁻³)	$\tilde{F}G_{\text{scatt}}/10^{-3}$ (pc ² km) ^{-1/3}	$\tilde{F}/10^{-4}$ (pc ² km) ^{-1/3}
J0357+5236	2.8×10^{-3}	49 ± 8	55 ± 8	5 ± 1	$6.1^{+4.4}_{-2.0}$
J0358+5413	3.5×10^{-4}	16 ± 3	41 ± 3	2.3 ± 0.4	$3.7^{+5.1}_{-1.5}$
J0601-0527	4.5×10^{-3}	27 ± 3	54 ± 3	15 ± 2	$6.4^{+1.6}_{-1.5}$
J1614-2230	1.6×10^{-4}	11 ± 1	24 ± 1	2.9 ± 0.4	$4.0^{+1.4}_{-1.3}$
J1643-1224	4.9×10^{-2}	12 ± 1	50 ± 1	270 ± 40	370^{+130}_{-100}

NOTE—Values of DM_{ISM} correspond to the DM contribution of the thick disk based on the best-fit plane-parallel model of Ocker et al. (2020), and the H II region contributions are estimated as DM_{HII} = DM_{tot} - DM_{ISM}. Errors correspond to the 15% and 85% confidence intervals. Errors on $\tilde{F}G_{\text{scatt}}$ include the uncertainty in DM_{HII} and an assumed 10% uncertainty in τ . Errors on \tilde{F} further include uncertainties in the distances of the pulsars and H II regions, which in turn yield uncertainties on the pulsars’ path lengths through the H II regions; these estimates assume that the entire path through the H II region contributes to scattering, which may not be the case. The fluctuation parameter conventionally used to estimate scattering measures, $F_c = \tilde{F}l_i^{1/3}$, would be $10 \times \tilde{F}$ for $l_i = 10^3$ km.

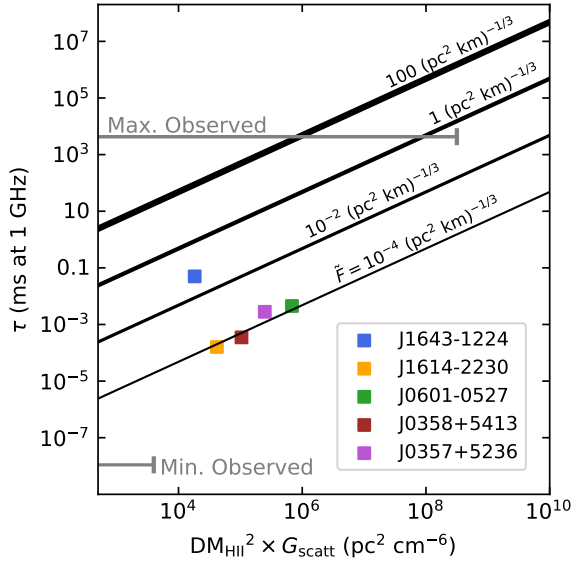


Figure 9. Scattering delay τ in ms at 1 GHz vs. $\text{DM}_{\text{HII}}^2 \times G_{\text{scatt}}$, for four different values of the density fluctuation parameter \tilde{F} (black solid lines). Colored squares indicate the inferred values of $\text{DM}_{\text{HII}}^2 \times G_{\text{scatt}}$ for the five pulsars with parallax distances that intersect H II regions, which yield the values of \tilde{F} shown in Table 3 if the H II regions dominate the observed scattering. The largest and smallest published scattering delays are shown by the grey horizontal lines, corresponding to PSRs J1550-5418 ($\tau_{1\text{GHz}} \approx 4000$ ms) and J0953+0755 ($\tau_{1\text{GHz}} \approx 1 \times 10^{-8}$ ms). For these two extremes in τ we show conservative upper limits on $\text{DM}^2 G_{\text{scatt}}$ that assume the total observed DM comes from a scattering screen halfway between the source and observer, and a screen width $\sim 0.1\%$ of the distance to the source. J1550-5418 intersects at least one H II region, and its observed scattering can be explained for reasonable values of $\text{DM}_{\text{HII}}^2 \times G_{\text{scatt}}$ if \tilde{F} is $\gtrsim 1$ (pc² km)^{-1/3}.

J0358+5236, at least three other scattering screens are located beyond the H II region (Ocker et al. 2024), and for J1643-1224 there may be one additional screen beyond the H II region (Mall et al. 2022). In principle, such observations could be used to constrain the amount of scattering contributed by each screen along the LOS, including the specific scattering contributions of the H II regions, but such studies are complicated by a variety of effects that modify the observed scintillation, including but not limited to radio-frequency dependence (typically one or two screens dominate scintillation at low frequencies, whereas many more screens contribute at higher frequencies). Scintillation observations of pulsars at distances < 400 pc suggest that the DM contributions of scattering screens associated with scintillation arcs are extremely small, because many screens are detected for pulsars with total DMs < 5 pc cm⁻³ (Ocker et al. 2024; D. Reardon et al., in review). These results may support a scenario in which variations in \tilde{F} (and G_{scatt}) dominate variations in τ , although the degree to which results from pulsar scintillation arcs are applicable to more distant pulsars in the high-DM, high- τ regime remains unclear, given that scintillation arcs tend to be observable only for nearby, lower DM pulsars (Stinebring et al. 2022; Main et al. 2023).

7. DISCUSSION

Our study has been limited thus far to comparing the pulsar population to H II regions with distances, which only constitute $\approx 1/3$ of the ≈ 8400 sources in the WISE Catalog (the vast majority of which are likely bona fide H II regions; § 2). To illustrate the potential impact of the full H II region population on pulsar observables, we estimate both the areal covering fraction of H II regions and the maximum possible DM contribution of H II regions as functions of Galactic longitude. The top panel of Figure 10 shows the areal covering fraction of all regions in the WISE Catalog at Galactic lati-

tudes $|b| < 2^\circ$, based on the angular radii (θ_{HII}) given in the catalog. Using the cataloged θ_{HII} , we find an areal covering fraction that is $\approx 20\%$ across much of the inner Galaxy. Using the larger angular extent ($2\theta_{\text{HII}}$) assumed in our intersection analysis yields an areal covering fraction $\approx 50\%$ across the inner Galaxy, although the covering fraction varies substantially with longitude and in some cases is $> 80\%$ (notably rising to $> 100\%$ around the Cygnus region). The bottom panel of Figure 10 shows simulated estimates of the maximum possible DM from H II regions for extragalactic LOSs at $|b| < 2^\circ$. We estimate the maximum DM by sampling 5000 LOSs uniformly distributed over all Galactic longitudes and identifying the H II regions in the WISE Catalog that every LOS intersects (within $2\theta_{\text{HII}}$, as in our earlier analysis). Each H II region’s distance is randomly drawn from a uniform distribution spanning 1 to 10 kpc, and the LOS path length through each intersected H II region is evaluated from the LOS impact parameter and H II region distance. For illustrative purposes, the maximum DM distribution is then binned by every 2° in longitude. Figure 10 shows the resulting DM integrated through all intervening H II regions, for two mean electron densities describing the H II region interiors: 1 cm^{-3} and 5 cm^{-3} . This simulation does not include the DM contribution of the ISM, which is why the DM distribution shown in Figure 10 drops to 0 pc cm^{-3} for some LOSs. When compared to the observed DMs of Galactic pulsars and the maximum DM predicted by NE2001, this simple simulation suggests that even for a modest electron density (1 cm^{-3}), H II regions could account for 20 – 25% of the total DM in the Galactic plane for longitudes $|l| \lesssim 70^\circ$, and that for $|l| > 70^\circ$ H II regions can contribute the majority of DM. Allowing for larger interior densities would imply that H II regions account for a much higher fraction ($\gtrsim 50\%$) of the total DM.

Our results suggest that H II regions form a significant constituent of the electron density content probed by the pulsar population. Accounting for H II regions is thus critical to understanding present-day uncertainties in Galactic electron density models, which are the primary tool for estimating distances to both pulsars and fast radio bursts (FRBs) that lack independent distance measures. Galactic electron density models are fundamental to a broad range of studies; within pulsar astronomy alone, the distances inferred from these models are used to characterize the pulsar velocity distribution (Arzoumanian et al. 2002) and underlying dynamics at birth (Hansen & Phinney 1997), estimate the formation rate of double neutron star systems (Narayan et al. 1991), constrain the Shklovskii effect in pulsar timing (Shklovskii 1970), and test perturbations to General Relativity (Kramer et al. 2006). These examples are only a handful of the purposes for which Galactic electron density mod-

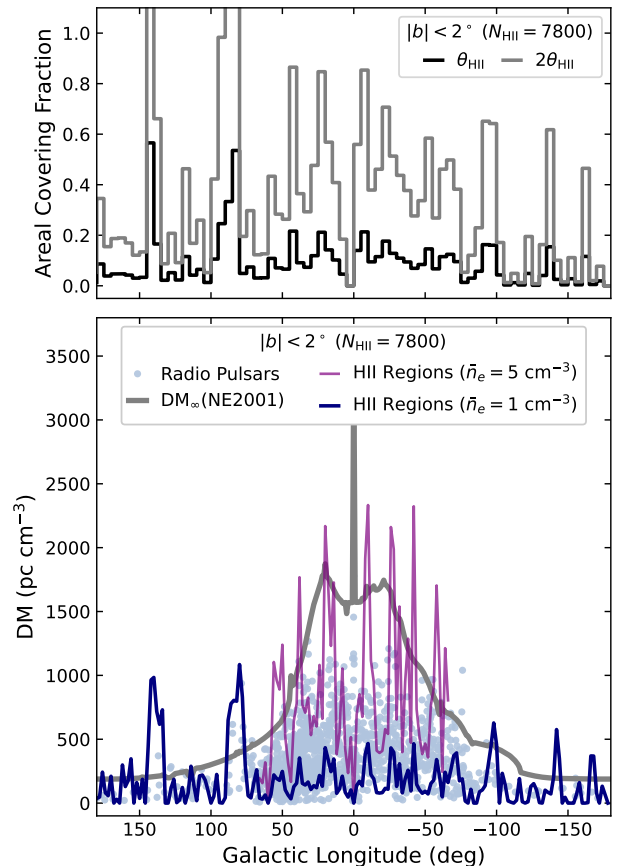


Figure 10. *Top:* Areal covering fraction vs. Galactic longitude of ≈ 7800 H II regions in the WISE Catalog at Galactic latitudes $|b| < 2^\circ$. The areal covering fraction is evaluated in 5° wide longitude bins using the angular radii given by the WISE Catalog (θ_{HII} ; black line) and twice the angular radii ($2\theta_{\text{HII}}$; grey line). *Bottom:* Simulation of the maximum DM contribution vs. Galactic longitude from all H II regions in the WISE Catalog at $|b| < 2^\circ$. The dark blue curve gives the maximum possible DM for LOSs passing within $2\theta_{\text{HII}}$ of H II regions, assuming that H II regions are described by a mean electron density $\bar{n}_e = 1 \text{ cm}^{-3}$. The purple curve shows the maximum possible DM from H II regions assuming $\bar{n}_e = 5 \text{ cm}^{-3}$, restricted to longitudes $|l| < 70^\circ$ to illustrate how with larger densities, H II regions could account for a significant fraction of DMs in the inner Galaxy. The distribution of DMs for radio pulsars at $|b| < 2^\circ$ is shown by the light blue points, and the maximum DM predicted by NE2001 at $b = 0^\circ$ is shown by the solid grey curve.

els have been used, and the model uncertainties have correspondingly broad implications.

H II regions should be incorporated into a next-generation Galactic electron density model. While early electron density models of the local ISM inferred pulsar distances based on a statistical distribution of H II regions (Prentice & Ter Haar 1969), modern electron density models based on pulsars do not explicitly include the known H II region population, which is effectively subsumed into spiral arm compo-

nents. Evidence for the electron density structure of the spiral arms is inferred from a spatially-dependent deficit in the DM predicted by smooth models that lack spiral arms (Taylor & Cordes 1993; Gómez et al. 2001). Spiral arms are included in models such as NE2001 and YMW16 as smooth overdensities, and to account for inhomogeneities in the arms due to, e.g., star-forming regions, H II regions, supershells, and supernova remnants, NE2001 includes LOS-specific clumps and voids that are required to explain certain DM and scattering measurements. Some of the clumps used in NE2001 include H II regions identified in our analysis. YMW16 does not include specific clumps or voids whatsoever. Most of these prior models suggested that H II regions are not statistically significant contributors to the DM and scattering of the observed pulsar population.

Our findings leave a potential dilemma for future electron density models. H II regions could be included on a case-by-case basis, as done previously for TC93 and NE2001, or a spiral arm model could be constructed to directly mimic the known H II region population. In practice, both of these options would be cumbersome to employ. The former option would require calibrating the DM and scattering contributions of up to 100s of H II regions on a pulsar-by-pulsar basis. The latter option would likely involve constructing a ‘universal’ H II region model that accounts for a range of H II region sizes and interior densities, which would need to be calibrated against 100s of pulsars with known distances intersecting H II regions at a range of impact parameters. We are actively considering these various approaches, and H II regions with the most extreme DM and scattering contributions will be added on a case-by-case basis to an in progress, extended version of NE2001p (Ocker & Cordes 2024).

Regardless of how future electron density models are constructed, the known H II region population can be used to constrain uncertainties in the currently used models. In general, LOSs with foreground H II regions will tend to have distances that are overestimated by NE2001 and YMW16, because the models have to integrate to larger distances to match the observed DM. However, the tendency to over- or under-estimate distances will be spatially dependent. Figure 4 compares the spiral arm components used in NE2001 to the sample of H II regions with distances in WISE and HH14 and the spiral arm parameters fit to maser parallaxes by Reid et al. (2019). In the second and third Galactic quadrants (around the Galactic anti-center), NE2001 places spiral arms at larger distances from the Sun than the Reid et al. (2019) arms, suggesting that pulsars in these regions will have overestimated distances. Conversely, in the third and fourth Galactic quadrants NE2001 places portions of the Carina-Sagittarius and Crux-Scutum arms closer to the Sun than Reid et al. (2019), suggesting that pulsars with LOSs tangent to those arms will tend to have underestimated dis-

tances in those quadrants. While the spiral arm locations of both NE2001 and Reid et al. (2019) have substantial uncertainties, the H II region locations in Figure 4 are more consistent with the Reid et al. (2019) arms. All log-periodic spiral arm models are idealized, approximate views of the Milky Way’s global structure, and the exact number of primary arms and roles of kinks and bifurcations remain subject to disagreement (e.g. Xu et al. 2023; Denyshchenko et al. 2024). Such problems would be largely alleviated if the observed pulsar population reaches the critical mass needed to directly perform tomography of the ionized ISM.

In addition to their use as distance estimators, Galactic models are critical to constraining the FRB Galactic foreground, which induces noise in FRB-based inferences of both host galaxy and intergalactic medium (IGM) properties (Petroff et al. 2019; Cordes & Chatterjee 2019). While FRB surveys have historically prioritized high Galactic latitudes, where H II regions are rare, current and future surveys inevitably cover low latitudes where uncertainties in Galactic models exacerbate the identification of local universe FRBs with ambiguously small DMs (Ravi et al. 2023), which also provide the most stringent constraints on FRB source models (e.g. Bhardwaj et al. 2021; Kirsten et al. 2022). Simultaneous searches for both new pulsars and radio bursts from Galactic magnetars are also most successful in the plane (Bochenek et al. 2020; CHIME/FRB Collaboration et al. 2020; Good et al. 2021; Dong et al. 2023), and these latitudes will be increasingly important as surveys like DSA-2000 (Hallinan et al. 2019; Ravi et al. 2019) and CHORD (Vanderlinde et al. 2019) expand the sensitivity phase space for pulsar, magnetar, and FRB discovery. Figure 2 gives a rough indication of the degree of ‘noise’ that H II regions contribute to the Galactic DM foreground as a function of Galactic longitude; it is already apparent from this figure that there are certain regions of the sky where FRB surveys are more likely to misidentify Galactic sources as extragalactic, because Galactic electron density models are used to distinguish between Galactic and extragalactic FRB candidates.

H II regions are also important for interpreting FRB host galaxy contributions to DM. When the host galaxy inclination angle is large (edge-on), then H II regions can contribute 10s to 100s pc cm^{-3} to the host DM, depending on the FRB location. $\text{H}\alpha$ EMs are frequently used as an alternative predictor of the host DM contribution, even though these EMs are based on single-slit measurements that integrate over the whole galaxy (Tendulkar et al. 2017; Ocker et al. 2022). Understanding the degree to which H II regions vs. the diffuse ISM contribute to the observed $\text{H}\alpha$ intensity may be especially relevant when the host DM appears to be large (or small) relative to the observed $\text{H}\alpha$ emission, because it is typically unclear whether the FRB’s circumsource medium (e.g., a supernova remnant or wind nebula) contributes signif-

icantly to the host DM (Ocker et al. 2022; Caleb et al. 2022). Similarly, constraints on the density fluctuation parameter \tilde{F} in host galaxies typically assume that the FRB scattering arises from the host’s extended ISM (Cordes et al. 2022; Ocker et al. 2022; Cassanelli et al. 2023; Caleb et al. 2023), but for high host inclination angles, one or a few H II regions could dominate the scattering contribution of the host.

8. SUMMARY

We have shown that the majority of pulsars with $DM > 600 \text{ pc cm}^{-3}$ and $\tau > 10 \text{ ms}$ at 1 GHz intersect H II regions with distances in the WISE and HH14 catalogs, and that nearly all pulsars with DMs greater than the maximum predictions of NE2001 and YMW16 lie behind H II regions. For a subset of about 500 pulsars with scattering measurements, we have individually assessed the validity of identified intersections and found a false positive rate of about 20% and a false negative rate $\leq 30\%$. A catalog of the pulsar and H II region pairs is provided in Appendix A; these pulsars would be prime follow-up targets for Faraday RM studies. Intersections were likely missed because they were identified using only H II regions with published distances, and because of the assumed impact parameter cutoff. Combined with the number of validated intersections, the false positive and negative rates suggest that as much as a third of the known pulsar population may intersect H II regions. Due to selection effects that bias the intersection sample towards LOSs through the inner Galaxy, we anticipate that more intersections for pulsar DMs $< 600 \text{ pc cm}^{-3}$ will be found as the sample of both pulsar and H II region distances increases. A detailed examination of pulsar LOSs and H II regions covered by radio recombination maps suggests that H II regions contribute

10s to 100s of pc cm^{-3} in electron column, depending on the LOS. Our assessment of pulsar scattering measurements suggests that if H II regions dominate the scattering of background pulsars, then the density fluctuations parameterized by \tilde{F} must vary significantly between H II regions. Simulating the full H II region population assuming a modest interior electron density suggests that at low latitudes, H II regions can account for $\gtrsim 20\%$ of the total DM contribution of the Galactic disk, and that for some LOSs (e.g. near the Cygnus region), H II regions contribute the majority of free electrons along the LOS.

These results can be directly tested by cross-correlating pulsar LOSs spanning a range of impact parameters through H II regions with detailed spectroscopic information, which will constrain any relation between H II region properties and the turbulent density fluctuations probed by pulsar scattering, in addition to yielding the mean electron density profiles of H II regions around different ionizing star types. Such science cases may soon be achievable with the SDSS-V Local Volume Mapper (Drory et al. 2024).

ACKNOWLEDGMENTS

SKO is supported by the Brinson Foundation through the Brinson Prize Fellowship Program. SKO, JL, and JMC are members of the NANOGrav Physics Frontiers Center (NSF award PHY-2020265). SKO is grateful to Liam Connor, Casey Law, Kritti Sharma, Jakob Faber, Myles Sherman, Nikita Gosogorov, and Nick Konidaris for fruitful discussions, and to Jack Madden for lending his eyes to Figure 5. Caltech and Carnegie Observatories are located on the traditional and unceded lands of the Tongva people.

REFERENCES

- Agazie, G., Anumarlapudi, A., Archibald, A. M., et al. 2023, *ApJL*, 951, L10, doi: [10.3847/2041-8213/acda88](https://doi.org/10.3847/2041-8213/acda88)
- Alves, M. I. R., Calabretta, M., Davies, R. D., et al. 2015, *MNRAS*, 450, 2025, doi: [10.1093/mnras/stv751](https://doi.org/10.1093/mnras/stv751)
- Anantharamaiah, K. R., & Narayan, R. 1988, in *American Institute of Physics Conference Series*, Vol. 174, *Radio Wave Scattering in the Interstellar Medium*, ed. J. M. Cordes, B. J. Rickett, & D. C. Backer (AIP), 185–189, doi: [10.1063/1.37590](https://doi.org/10.1063/1.37590)
- Anderson, L. D., Armentrout, W. P., Johnstone, B. M., et al. 2015, *ApJS*, 221, 26, doi: [10.1088/0067-0049/221/2/26](https://doi.org/10.1088/0067-0049/221/2/26)
- Anderson, L. D., Armentrout, W. P., Luisi, M., et al. 2018, *ApJS*, 234, 33, doi: [10.3847/1538-4365/aa956a](https://doi.org/10.3847/1538-4365/aa956a)
- Anderson, L. D., Bania, T. M., Balsler, D. S., et al. 2014, *ApJS*, 212, 1, doi: [10.1088/0067-0049/212/1/1](https://doi.org/10.1088/0067-0049/212/1/1)
- Anderson, L. D., Bania, T. M., Balsler, D. S., & Rood, R. T. 2011, *ApJS*, 194, 32, doi: [10.1088/0067-0049/194/2/32](https://doi.org/10.1088/0067-0049/194/2/32)
- Anderson, L. D., Zavagno, A., Barlow, M. J., García-Lario, P., & Noriega-Crespo, A. 2012, *A&A*, 537, A1, doi: [10.1051/0004-6361/201117640](https://doi.org/10.1051/0004-6361/201117640)
- Anderson, L. D., Luisi, M., Liu, B., et al. 2021, *ApJS*, 254, 28, doi: [10.3847/1538-4365/abef65](https://doi.org/10.3847/1538-4365/abef65)
- Armentrout, W. P., Anderson, L. D., Wenger, T. V., Balsler, D. S., & Bania, T. M. 2021, *ApJS*, 253, 23, doi: [10.3847/1538-4365/abd5c0](https://doi.org/10.3847/1538-4365/abd5c0)
- Arzoumanian, Z., Chernoff, D. F., & Cordes, J. M. 2002, *ApJ*, 568, 289, doi: [10.1086/338805](https://doi.org/10.1086/338805)
- Azcárate, I. N., Cersosimo, J. C., Wilkes, L. M., & Cordero, Y. A. 1997, *Astrophysics & Space Science*, 253, 313, doi: [10.1023/A:1000715203886](https://doi.org/10.1023/A:1000715203886)
- Bania, T. M., Anderson, L. D., & Balsler, D. S. 2012, *ApJ*, 759, 96, doi: [10.1088/0004-637X/759/2/96](https://doi.org/10.1088/0004-637X/759/2/96)
- Bania, T. M., Anderson, L. D., Balsler, D. S., & Rood, R. T. 2010, *ApJL*, 718, L106, doi: [10.1088/2041-8205/718/2/L106](https://doi.org/10.1088/2041-8205/718/2/L106)

- Barcia, A., Gomez-Gonzalez, J., Lockman, F. J., & Planesas, P. 1985, *A&A*, 147, 237
- Bhardwaj, M., Gaensler, B. M., Kaspi, V. M., et al. 2021, *ApJL*, 910, L18, doi: [10.3847/2041-8213/abeaa6](https://doi.org/10.3847/2041-8213/abeaa6)
- Bhat, N. D. R., Cordes, J. M., Camilo, F., Nice, D. J., & Lorimer, D. R. 2004, *ApJ*, 605, 759, doi: [10.1086/382680](https://doi.org/10.1086/382680)
- Bochenek, C. D., Ravi, V., Belov, K. V., et al. 2020, *Nature*, 587, 59, doi: [10.1038/s41586-020-2872-x](https://doi.org/10.1038/s41586-020-2872-x)
- Caleb, M., Heywood, I., Rajwade, K., et al. 2022, *Nature Astronomy*, 6, 828, doi: [10.1038/s41550-022-01688-x](https://doi.org/10.1038/s41550-022-01688-x)
- Caleb, M., Driessen, L. N., Gordon, A. C., et al. 2023, *MNRAS*, 524, 2064, doi: [10.1093/mnras/stad1839](https://doi.org/10.1093/mnras/stad1839)
- Cassanelli, T., Leung, C., Sanghavi, P., et al. 2023, arXiv e-prints, arXiv:2307.09502, doi: [10.48550/arXiv.2307.09502](https://doi.org/10.48550/arXiv.2307.09502)
- Caswell, J. L., & Haynes, R. F. 1987, *A&A*, 171, 261
- CHIME/FRB Collaboration, Andersen, B. C., Bandura, K. M., et al. 2020, *Nature*, 587, 54, doi: [10.1038/s41586-020-2863-y](https://doi.org/10.1038/s41586-020-2863-y)
- Cordes, J. M., & Chatterjee, S. 2019, *ARAA*, 57, 417, doi: [10.1146/annurev-astro-091918-104501](https://doi.org/10.1146/annurev-astro-091918-104501)
- Cordes, J. M., & Lazio, T. J. W. 2002, arXiv e-prints, astro. <https://arxiv.org/abs/astro-ph/0207156>
- . 2003, arXiv e-prints, astro. <https://arxiv.org/abs/astro-ph/0301598>
- Cordes, J. M., Ocker, S. K., & Chatterjee, S. 2022, *ApJ*, 931, 88, doi: [10.3847/1538-4357/ac6873](https://doi.org/10.3847/1538-4357/ac6873)
- Cordes, J. M., Weisberg, J. M., Frail, D. A., Spangler, S. R., & Ryan, M. 1991, *Nature*, 354, 121, doi: [10.1038/354121a0](https://doi.org/10.1038/354121a0)
- Cordes, J. M., Wharton, R. S., Spitler, L. G., Chatterjee, S., & Wasserman, I. 2016, arXiv e-prints, arXiv:1605.05890. <https://arxiv.org/abs/1605.05890>
- Cordes, J. M., Freire, P. C. C., Lorimer, D. R., et al. 2006, *ApJ*, 637, 446, doi: [10.1086/498335](https://doi.org/10.1086/498335)
- Deller, A. T., Goss, W. M., Brisken, W. F., et al. 2019, *ApJ*, 875, 100, doi: [10.3847/1538-4357/ab11c7](https://doi.org/10.3847/1538-4357/ab11c7)
- Denyshchenko, S. I., Fedorov, P. N., Akhmetov, V. S., Velichko, A. B., & Dmytrenko, A. M. 2024, *MNRAS*, 527, 1472, doi: [10.1093/mnras/stad3350](https://doi.org/10.1093/mnras/stad3350)
- Ding, H., Deller, A. T., Stappers, B. W., et al. 2023, *MNRAS*, 519, 4982, doi: [10.1093/mnras/stac3725](https://doi.org/10.1093/mnras/stac3725)
- Dong, F. A., Crowter, K., Meyers, B. W., et al. 2023, *MNRAS*, 524, 5132, doi: [10.1093/mnras/stad2012](https://doi.org/10.1093/mnras/stad2012)
- Draine, B. T. 2011, *Physics of the Interstellar and Intergalactic Medium* (Princeton University Press)
- Drory, N., Blanc, G. A., Kreckel, K., et al. 2024, arXiv e-prints, arXiv:2405.01637, doi: [10.48550/arXiv.2405.01637](https://doi.org/10.48550/arXiv.2405.01637)
- Dunham, M. K., Rosolowsky, E., Evans, Neal J., I., Cyganowski, C., & Urquhart, J. S. 2011, *ApJ*, 741, 110, doi: [10.1088/0004-637X/741/2/110](https://doi.org/10.1088/0004-637X/741/2/110)
- EPTA Collaboration, InPTA Collaboration, Antoniadis, J., et al. 2023, *A&A*, 678, A49, doi: [10.1051/0004-6361/202346842](https://doi.org/10.1051/0004-6361/202346842)
- Fich, M., Treffers, R. R., & Dahl, G. P. 1990, *AJ*, 99, 622, doi: [10.1086/115356](https://doi.org/10.1086/115356)
- Foster, T., & Brunt, C. M. 2015, *AJ*, 150, 147, doi: [10.1088/0004-6256/150/5/147](https://doi.org/10.1088/0004-6256/150/5/147)
- Frail, D. A., & Weisberg, J. M. 1990, *AJ*, 100, 743, doi: [10.1086/115556](https://doi.org/10.1086/115556)
- Gao, X. Y., Reich, P., Hou, L. G., Reich, W., & Han, J. L. 2019, *A&A*, 623, A105, doi: [10.1051/0004-6361/201834092](https://doi.org/10.1051/0004-6361/201834092)
- Gómez, G. C., Benjamin, R. A., & Cox, D. P. 2001, *AJ*, 122, 908, doi: [10.1086/321180](https://doi.org/10.1086/321180)
- Good, D. C., Andersen, B. C., Chawla, P., et al. 2021, *ApJ*, 922, 43, doi: [10.3847/1538-4357/ac1da6](https://doi.org/10.3847/1538-4357/ac1da6)
- Gordon, M. A., & Sorochenko, R. L. 2002, *Radio Recombination Lines. Their Physics and Astronomical Applications*, Vol. 282, doi: [10.1007/978-0-387-09604-9](https://doi.org/10.1007/978-0-387-09604-9)
- Gum, C. S. 1955, *Memoirs of the Royal Astronomical Society*, 67, 155
- Hallinan, G., Ravi, V., Weinreb, S., et al. 2019, in *Bulletin of the American Astronomical Society*, Vol. 51, 255, doi: [10.48550/arXiv.1907.07648](https://doi.org/10.48550/arXiv.1907.07648)
- Han, J. L., Wang, C., Wang, P. F., et al. 2021, *Research in Astronomy and Astrophysics*, 21, 107, doi: [10.1088/1674-4527/21/5/107](https://doi.org/10.1088/1674-4527/21/5/107)
- Hansen, B. M. S., & Phinney, E. S. 1997, *MNRAS*, 291, 569, doi: [10.1093/mnras/291.3.569](https://doi.org/10.1093/mnras/291.3.569)
- Harvey-Smith, L., Madsen, G. J., & Gaensler, B. M. 2011, *ApJ*, 736, 83, doi: [10.1088/0004-637X/736/2/83](https://doi.org/10.1088/0004-637X/736/2/83)
- Haverkorn, M., Gaensler, B. M., McClure-Griffiths, N. M., Dickey, J. M., & Green, A. J. 2004, *ApJ*, 609, 776, doi: [10.1086/421341](https://doi.org/10.1086/421341)
- Heiles, C., Reach, W. T., & Koo, B.-C. 1996, *ApJ*, 466, 191, doi: [10.1086/177503](https://doi.org/10.1086/177503)
- Hou, L., Han, J., Hong, T., Gao, X., & Wang, C. 2022, *Science China Physics, Mechanics, and Astronomy*, 65, 129703, doi: [10.1007/s11433-022-2039-8](https://doi.org/10.1007/s11433-022-2039-8)
- Hou, L. G., & Han, J. L. 2014, *A&A*, 569, A125, doi: [10.1051/0004-6361/201424039](https://doi.org/10.1051/0004-6361/201424039)
- Johnston, S., Karastergiou, A., Keith, M. J., et al. 2020, *MNRAS*, 493, 3608, doi: [10.1093/mnras/staa516](https://doi.org/10.1093/mnras/staa516)
- Kirsten, F., Marcote, B., Nimmo, K., et al. 2022, *Nature*, 602, 585, doi: [10.1038/s41586-021-04354-w](https://doi.org/10.1038/s41586-021-04354-w)
- Kramer, M., Stairs, I. H., Manchester, R. N., et al. 2006, *Science*, 314, 97, doi: [10.1126/science.1132305](https://doi.org/10.1126/science.1132305)
- Krishnakumar, M. A., Mitra, D., Naidu, A., Joshi, B. C., & Manoharan, P. K. 2015, *ApJ*, 804, 23, doi: [10.1088/0004-637X/804/1/23](https://doi.org/10.1088/0004-637X/804/1/23)
- Lazio, T. J., Spangler, S. R., & Cordes, J. M. 1990, *ApJ*, 363, 515, doi: [10.1086/169362](https://doi.org/10.1086/169362)
- Liu, B., Anderson, L. D., McIntyre, T., et al. 2019, *ApJS*, 240, 14, doi: [10.3847/1538-4365/aaef8e](https://doi.org/10.3847/1538-4365/aaef8e)
- Lockman, F. J. 1989, *ApJS*, 71, 469, doi: [10.1086/191383](https://doi.org/10.1086/191383)

- Lockman, F. J., Pisano, D. J., & Howard, G. J. 1996, *ApJ*, 472, 173, doi: [10.1086/178052](https://doi.org/10.1086/178052)
- Luisi, M., Anderson, L. D., Liu, B., Anish Roshi, D., & Churchwell, E. 2019, *ApJS*, 241, 2, doi: [10.3847/1538-4365/aaf6a5](https://doi.org/10.3847/1538-4365/aaf6a5)
- Main, R. A., Parthasarathy, A., Johnston, S., et al. 2023, *MNRAS*, 518, 1086, doi: [10.1093/mnras/stac3149](https://doi.org/10.1093/mnras/stac3149)
- Mall, G., Main, R. A., Antoniadis, J., et al. 2022, *MNRAS*, 511, 1104, doi: [10.1093/mnras/stac096](https://doi.org/10.1093/mnras/stac096)
- Manchester, R. N., Hobbs, G. B., Teoh, A., & Hobbs, M. 2005, *AJ*, 129, 1993, doi: [10.1086/428488](https://doi.org/10.1086/428488)
- McKee, C. F., & Williams, J. P. 1997, *ApJ*, 476, 144, doi: [10.1086/303587](https://doi.org/10.1086/303587)
- Mitra, D., Wielebinski, R., Kramer, M., & Jessner, A. 2003, *A&A*, 398, 993, doi: [10.1051/0004-6361:20021702](https://doi.org/10.1051/0004-6361:20021702)
- Narayan, R., Piran, T., & Shemi, A. 1991, *ApJL*, 379, L17, doi: [10.1086/186143](https://doi.org/10.1086/186143)
- Ochsenbein, F., Bauer, P., & Marcout, J. 2000, *A&AS*, 143, 23, doi: [10.1051/aas:2000169](https://doi.org/10.1051/aas:2000169)
- Ocker, S. K., & Cordes, J. M. 2024, *Research Notes of the American Astronomical Society*, 8, 17, doi: [10.3847/2515-5172/ad1bf1](https://doi.org/10.3847/2515-5172/ad1bf1)
- Ocker, S. K., Cordes, J. M., & Chatterjee, S. 2020, *ApJ*, 897, 124, doi: [10.3847/1538-4357/ab98f9](https://doi.org/10.3847/1538-4357/ab98f9)
- . 2021, *ApJ*, 911, 102, doi: [10.3847/1538-4357/abeb6e](https://doi.org/10.3847/1538-4357/abeb6e)
- Ocker, S. K., Cordes, J. M., Chatterjee, S., et al. 2022, *ApJ*, 931, 87, doi: [10.3847/1538-4357/ac6504](https://doi.org/10.3847/1538-4357/ac6504)
- . 2024, *MNRAS*, 527, 7568, doi: [10.1093/mnras/stad3683](https://doi.org/10.1093/mnras/stad3683)
- Oswald, L. S., Karastergiou, A., Posselt, B., et al. 2021, *MNRAS*, 504, 1115, doi: [10.1093/mnras/stab980](https://doi.org/10.1093/mnras/stab980)
- Pan, Z., Qian, L., Ma, X., et al. 2021, *ApJL*, 915, L28, doi: [10.3847/2041-8213/ac0bbd](https://doi.org/10.3847/2041-8213/ac0bbd)
- Parent, E., Sewalls, H., Freire, P. C. C., et al. 2022, *ApJ*, 924, 135, doi: [10.3847/1538-4357/ac375d](https://doi.org/10.3847/1538-4357/ac375d)
- Petroff, E., Hessels, J. W. T., & Lorimer, D. R. 2019, *AAPR*, 27, 4, doi: [10.1007/s00159-019-0116-6](https://doi.org/10.1007/s00159-019-0116-6)
- Posselt, B., Karastergiou, A., Johnston, S., et al. 2023, *MNRAS*, 520, 4582, doi: [10.1093/mnras/stac3383](https://doi.org/10.1093/mnras/stac3383)
- Prentice, A. J. R., & Ter Haar, D. 1969, *MNRAS*, 146, 423, doi: [10.1093/mnras/146.4.423](https://doi.org/10.1093/mnras/146.4.423)
- Price, D. C., Flynn, C., & Deller, A. 2021, *PASA*, 38, e038, doi: [10.1017/pasa.2021.33](https://doi.org/10.1017/pasa.2021.33)
- Quireza, C., Rood, R. T., Balser, D. S., & Bania, T. M. 2006a, *ApJS*, 165, 338, doi: [10.1086/503901](https://doi.org/10.1086/503901)
- Quireza, C., Rood, R. T., Bania, T. M., Balser, D. S., & Maciel, W. J. 2006b, *ApJ*, 653, 1226, doi: [10.1086/508803](https://doi.org/10.1086/508803)
- Ravi, V., Battaglia, N., Burke-Spolaor, S., et al. 2019, *BAAS*, 51, 420, doi: [10.48550/arXiv.1903.06535](https://doi.org/10.48550/arXiv.1903.06535)
- Ravi, V., Catha, M., Chen, G., et al. 2023, *arXiv e-prints*, arXiv:2301.01000, doi: [10.48550/arXiv.2301.01000](https://doi.org/10.48550/arXiv.2301.01000)
- Reardon, D. J., Zic, A., Shannon, R. M., et al. 2023, *ApJL*, 951, L7, doi: [10.3847/2041-8213/acdd03](https://doi.org/10.3847/2041-8213/acdd03)
- Reid, M. J., Menten, K. M., Brunthaler, A., et al. 2019, *ApJ*, 885, 131, doi: [10.3847/1538-4357/ab4a11](https://doi.org/10.3847/1538-4357/ab4a11)
- Rickett, B., Johnston, S., Tomlinson, T., & Reynolds, J. 2009, *MNRAS*, 395, 1391, doi: [10.1111/j.1365-2966.2009.14471.x](https://doi.org/10.1111/j.1365-2966.2009.14471.x)
- Rickett, B. J. 1990, *ARA&A*, 28, 561, doi: [10.1146/annurev.aa.28.090190.003021](https://doi.org/10.1146/annurev.aa.28.090190.003021)
- Rubin, R. H. 1968, *ApJ*, 154, 391, doi: [10.1086/149766](https://doi.org/10.1086/149766)
- Sharpless, S. 1959, *ApJS*, 4, 257, doi: [10.1086/190049](https://doi.org/10.1086/190049)
- Shklovskii, I. S. 1970, *SvA*, 13, 562
- Spangler, S. R. 1991, *ApJ*, 376, 540, doi: [10.1086/170303](https://doi.org/10.1086/170303)
- Spangler, S. R., & Cordes, J. M. 1998, *ApJ*, 505, 766, doi: [10.1086/306172](https://doi.org/10.1086/306172)
- Spangler, S. R., & Reynolds, R. J. 1990, *ApJ*, 361, 116, doi: [10.1086/169173](https://doi.org/10.1086/169173)
- Stinebring, D. R., McLaughlin, M. A., & Cordes, et al., J. M. 2001, *ApJL*, 549, L97, doi: [10.1086/319133](https://doi.org/10.1086/319133)
- Stinebring, D. R., Rickett, B. J., Minter, A. H., et al. 2022, *ApJ*, 941, 34, doi: [10.3847/1538-4357/ac8ea8](https://doi.org/10.3847/1538-4357/ac8ea8)
- Sun, X. H., Han, J. L., Reich, W., et al. 2007, *A&A*, 463, 993, doi: [10.1051/0004-6361:20066001](https://doi.org/10.1051/0004-6361:20066001)
- Sun, X. H., Reich, W., Han, J. L., et al. 2011, *A&A*, 527, A74, doi: [10.1051/0004-6361/201015383](https://doi.org/10.1051/0004-6361/201015383)
- Taylor, J. H., & Cordes, J. M. 1993, *ApJ*, 411, 674, doi: [10.1086/172870](https://doi.org/10.1086/172870)
- Tendulkar, S. P., Bassa, C. G., Cordes, J. M., et al. 2017, *ApJL*, 834, L7, doi: [10.3847/2041-8213/834/2/L7](https://doi.org/10.3847/2041-8213/834/2/L7)
- Urquhart, J. S., Morgan, L. K., Figura, C. C., et al. 2011, *MNRAS*, 418, 1689, doi: [10.1111/j.1365-2966.2011.19594.x](https://doi.org/10.1111/j.1365-2966.2011.19594.x)
- Urquhart, J. S., Hoare, M. G., Lumsden, S. L., et al. 2012, *MNRAS*, 420, 1656, doi: [10.1111/j.1365-2966.2011.20157.x](https://doi.org/10.1111/j.1365-2966.2011.20157.x)
- Vanderlinde, K., Liu, A., Gaensler, B., et al. 2019, in *Canadian Long Range Plan for Astronomy and Astrophysics White Papers*, Vol. 2020, 28, doi: [10.5281/zenodo.3765414](https://doi.org/10.5281/zenodo.3765414)
- Wenger, T. V., Dawson, J. R., Dickey, J. M., et al. 2021, *ApJS*, 254, 36, doi: [10.3847/1538-4365/abf4d4](https://doi.org/10.3847/1538-4365/abf4d4)
- Whiting, C. A., Spangler, S. R., Ingleby, L. D., & Haffner, L. M. 2009, *ApJ*, 694, 1452, doi: [10.1088/0004-637X/694/2/1452](https://doi.org/10.1088/0004-637X/694/2/1452)
- Wood, D. O. S., & Churchwell, E. 1989, *ApJS*, 69, 831, doi: [10.1086/191329](https://doi.org/10.1086/191329)
- Wright, E. L., Eisenhardt, P. R. M., Mainzer, A. K., et al. 2010, *AJ*, 140, 1868, doi: [10.1088/0004-6256/140/6/1868](https://doi.org/10.1088/0004-6256/140/6/1868)
- Xiao, L., Han, J. L., Reich, W., et al. 2011, *A&A*, 529, A15, doi: [10.1051/0004-6361/201016226](https://doi.org/10.1051/0004-6361/201016226)
- Xu, Y., Hao, C. J., Liu, D. J., et al. 2023, *ApJ*, 947, 54, doi: [10.3847/1538-4357/acc45c](https://doi.org/10.3847/1538-4357/acc45c)
- Yao, J. M., Manchester, R. N., & Wang, N. 2017, *ApJ*, 835, 29, doi: [10.3847/1538-4357/835/1/29](https://doi.org/10.3847/1538-4357/835/1/29)

APPENDIX

A. CATALOG OF PULSARS INTERSECTING H II REGIONS

Table A1 gives the full list of pulsars with scattering measurements that are identified as intersecting H II regions based on our selection criteria.

Table A1. Pulsars Intersecting H II Regions

Pulsar							H II Region				
Name	l	b	DM	τ	D	Method	l	b	D	Ref.	Notes
	($^{\circ}$)	($^{\circ}$)	(pc cm $^{-3}$)	(ms at 1 GHz)	(kpc)		($^{\circ}$)	($^{\circ}$)	(kpc)		
J0357 + 5236	149.099	-0.522	103.7	2.8×10^{-3}	3.33 ± 0.72	P	148.540	-0.240	0.85 ± 0.15	HH14	S205
J0358 + 5413	148.190	0.811	57.1	3.5×10^{-4}	1.10 ± 0.20	P	148.540	-0.240	0.85 ± 0.15	HH14	S205
J0601 - 0527	212.199	-13.481	80.5	4.5×10^{-3}	2.08 ± 0.17	P	213.704	-12.606	> 0.61	HH14	
J0837 - 4135	260.904	-0.336	147.2	1.0×10^{-2}	1.50 ± 0.45	Y	261.381	0.841	0.67 ± 0.17	HH14	
J0857 - 4424	265.457	0.822	184.4	0.11	2.83 ± 0.85	Y	265.151	1.454	0.91 ± 0.26	HH14	
J1046 - 5813	287.065	0.733	240.2	0.13	4.37 ± 1.31	N	287.247	0.355	2.50 ± 0.10	WISE	RCW52
J1056 - 6258	290.292	-2.966	320.6	0.45	2.99 ± 0.90	N	290.323	-2.983	[0.93, 4.74]	WISE	
J1114 - 6100	291.443	-0.321	676.7	21	15.48 ± 4.64	N	291.467	-0.142	7.20 ± 1.20	WISE	multiple
J1133 - 6250	294.213	-1.296	567.8	22	11.94 ± 3.58	N	294.793	-1.329	3.60 ± 0.60	WISE	multiple
J1138 - 6207	294.506	-0.463	518.9	26	9.56 ± 2.87	N	294.453	-0.520	[0.58, 6.20]	WISE	
J1305 - 6203	304.561	0.772	468.8	10	11.59 ± 3.48	Y	304.583	0.582	> 2.17	HH14	
J1316 - 6232	305.848	0.191	966.4	1.0×10^3	25.00 ± 7.50	Y	305.789	0.138	5.00 ± 0.10	WISE	multiple
J1327 - 6222	307.074	0.204	318.5	0.98	5.48 ± 1.64	N	308.653	-0.510	> 0.50	HH14	
J1338 - 6204	308.372	0.305	640.3	28	12.36 ± 3.71	Y	308.747	0.547	5.30 ± 0.80	WISE	
J1341 - 6220	308.730	-0.035	719.6	26	12.60 ± 3.78	Y	309.075	0.172	5.40 ± 1.20	WISE	
J1349 - 6130	309.813	0.587	283.9	6.4	5.48 ± 1.64	Y	309.905	0.373	5.50 ± 0.10	WISE	
J1359 - 6038	311.239	1.126	293.7	0.47	5.15 ± 1.54	N	312.305	0.663	> 0.94	HH14	
J1406 - 6121	311.841	0.203	537.3	48	8.09 ± 2.43	N	311.893	0.087	5.70 ± 2.40	WISE	multiple
J1412 - 6145	312.324	-0.366	512.5	19	7.79 ± 2.34	N	311.850	-0.540	1.50 ± 0.40	HH14	RCW83
J1413 - 6141	312.462	-0.337	667.6	42	10.01 ± 3.00	N	311.850	-0.540	1.50 ± 0.40	HH14	RCW83
J1511 - 5835	320.289	-0.508	329.4	23	5.12 ± 1.54	Y	320.109	-0.510	> 0.93	HH14	multiple
J1512 - 5759	320.772	-0.108	627.5	5.5	7.35 ± 2.20	N	320.893	-0.410	> 2.97	HH14	multiple
J1514 - 5925	320.284	-1.482	192.5	16	3.91 ± 1.17	Y	320.109	-0.510	> 0.93	HH14	multiple
J1527 - 5552	323.638	0.590	370.1	0.43	5.38 ± 1.61	Y	323.680	0.630	[3.00, 10.20]	WISE	
J1543 - 5459	326.025	-0.044	345.0	36	4.82 ± 1.45	N	326.474	-0.290	[3.54, 10.10]	WISE	
J1550 - 5418	327.237	-0.132	830.0	4.3×10^3	9.54 ± 2.86	N	326.985	-0.158	> 3.37	HH14	multiple
J1551 - 5310	328.033	0.669	491.6	1.3×10^2	7.51 ± 2.25	N	328.117	0.570	5.34 ± 0.40	WISE	
J1600 - 3053	344.090	16.451	52.3	1.2×10^{-2}	1.89 ± 0.57	Y	347.220	20.240	0.20 ± 0.40	HH14	S1
J1614 - 2230	352.636	20.192	34.5	1.6×10^{-4}	0.77 ± 0.05	P	349.840	22.260	0.20 ± 0.04	HH14	S7
J1614 - 5048	332.206	0.172	582.4	35	7.93 ± 2.38	N	332.275	-0.003	[3.10, 11.40]	WISE	
J1640 - 4715	337.713	-0.439	586.3	44	6.43 ± 1.93	N	337.684	-0.342	[2.90, 12.20]	WISE	
J1643 - 1224	5.669	21.218	62.4	4.9×10^{-2}	0.91 ± 0.08	P	6.280	23.580	0.20 ± 0.04	HH14	S27
J1644 - 4559	339.193	-0.195	478.7	11	5.09 ± 1.53	N	339.134	-0.376	3.00 ± 0.40	WISE	
J1707 - 4053	345.718	-0.197	351.8	46	4.46 ± 1.34	N	345.495	0.326	2.00 ± 0.25	HH14	
J1715 - 3859	348.194	-0.348	806.2	2.2×10^2	9.42 ± 2.83	N	348.691	-0.825	$3.40 \pm 0.30^{\dagger}$	WISE	RCW122
J1717 - 3425	352.120	2.025	583.5	16	25.00 ± 7.50	Y	352.440	2.260	1.00 ± 0.20	HH14	S10
J1717 - 3737	349.491	0.182	522.7	35	5.77 ± 1.73	N	350.000	0.200	1.60 ± 0.50	HH14	RCW125
J1720 - 3659	350.332	0.100	379.0	12	4.65 ± 1.39	N	350.000	0.200	1.60 ± 0.50	HH14	RCW125
J1721 - 3532	351.687	0.670	496.8	94	5.76 ± 1.73	N	351.662	0.518	$1.35 \pm 0.15^{\dagger}$	HH14	RCW128
J1722 - 3632	350.934	-0.001	416.2	9.8	4.44 ± 1.33	N	351.040	0.660	$1.35 \pm 0.15^{\dagger}$	HH14	S8
J1723 - 3659	350.682	-0.409	254.4	1.9	3.62 ± 1.09	N	350.991	-0.530	[2.90, 13.20]	WISE	

Table A1 continued

Table A1 (continued)

Pulsar							H II Region				
Name	l	b	DM	τ	D	Method	l	b	D	Ref.	Notes
	($^{\circ}$)	($^{\circ}$)	(pc cm^{-3})	(ms at 1 GHz)	(kpc)		($^{\circ}$)	($^{\circ}$)	(kpc)		
J1731 – 3123	356.233	1.354	354.5	15	7.29 ± 2.19	Y	355.890	1.610	1.20 ± 0.25	HH14	S13
J1745 – 2900	359.944	-0.047	1778.0	1.3×10^3	8.49 ± 2.54	N	359.964	-0.100	$5.52 \pm 1.05^{\dagger}$	WISE	multiple
J1745 – 2912	359.788	-0.175	1130.0	3.6×10^3	8.41 ± 2.52	N	359.757	-0.351	$2.67 \pm 0.16^{\dagger}$	WISE	multiple
J1746 – 2849	0.134	-0.030	1456.0	1.5×10^3	8.47 ± 2.54	N	0.320	-0.210	$2.92 \pm 0.41^{\dagger}$	WISE	S20
J1746 – 2856	0.126	-0.233	1168.0	7.4×10^2	8.43 ± 2.53	N	0.320	-0.210	$2.92 \pm 0.41^{\dagger}$	WISE	S20
J1753 – 2501	4.274	0.512	672.0	55	9.28 ± 2.78	N	4.290	0.550	1.30 ± 0.40	HH14	S22
J1757 – 2421	5.281	0.054	179.5	0.26	4.40 ± 1.32	N	5.332	0.081	[2.89, 13.40]	WISE	
J1801 – 2304	6.837	-0.066	1067.8	3.9×10^2	12.61 ± 3.78	N	6.979	-0.250	2.70 ± 0.80	HH14	
J1811 – 1736	12.821	0.435	473.9	46	5.99 ± 1.80	N	12.762	0.370	2.40 ± 0.20	HH14	S40
J1812 – 1718	13.109	0.538	251.4	31	4.15 ± 1.24	N	12.762	0.370	2.40 ± 0.20	HH14	S40
J1812 – 1733	12.904	0.387	509.8	59	6.32 ± 1.89	N	12.762	0.370	2.40 ± 0.20	HH14	S40
J1813 – 1749	12.816	-0.020	1087.0	4.1×10^3	12.05 ± 3.62	N	12.807	-0.204	2.40 ± 0.17	HH14	W33
J1816 – 1729	13.433	-0.424	520.7	14	6.46 ± 1.94	N	13.520	-0.410	$1.98 \pm 0.13^{\dagger}$	HH14	S43
J1818 – 1422	16.405	0.610	619.6	64	7.33 ± 2.20	N	16.936	0.758	2.00 ± 0.25	HH14	S49
J1820 – 1346	17.161	0.483	771.0	1.0×10^2	8.95 ± 2.69	N	17.144	0.765	2.00 ± 0.25	HH14	multiple
J1822 – 1400	17.252	-0.176	649.3	6.8	4.87 ± 1.46	N	17.250	-0.195	> 3.90	HH14	
J1823 – 1115	19.767	0.946	428.6	6.1	5.70 ± 1.71	N	18.426	1.922	[2.50, 13.00]	WISE	
J1824 – 1159	19.253	0.324	463.0	18	5.67 ± 1.70	N	19.485	0.138	2.00 ± 0.20	HH14	
J1824 – 1423	17.146	-0.796	427.6	12	5.70 ± 1.71	N	16.808	-1.072	$1.98 \pm 0.13^{\dagger}$	HH14	S50
J1825 – 1446	16.805	-1.001	352.2	21	5.16 ± 1.55	N	16.808	-1.072	$1.98 \pm 0.13^{\dagger}$	HH14	S50
J1826 – 1131	19.800	0.293	320.6	1.1	4.64 ± 1.39	N	18.725	-0.045	[4.30, 10.90]	WISE	
J1832 – 1021	21.587	-0.597	474.1	14	5.88 ± 1.76	N	21.902	-0.368	2.50 ± 0.40	HH14	multiple
J1833 – 0559	25.514	1.321	346.7	1.8×10^2	6.83 ± 2.05	Y	25.647	1.054	> 3.00	HH14	
J1833 – 0827	23.386	0.063	410.9	1.1	4.71 ± 1.41	N	23.115	0.556	1.70 ± 0.50	HH14	
J1835 – 0643	25.093	0.552	464.8	1.5×10^2	6.18 ± 1.85	N	24.919	0.294	$5.70 \pm 0.60^{\dagger}$	WISE	
J1837 – 0604	25.960	0.265	462.0	62	6.44 ± 1.93	N	25.700	0.031	2.67 ± 0.70	HH14	
J1841 – 0500	27.323	-0.034	532.0	2.2×10^3	7.04 ± 2.11	N	27.281	-0.131	5.50 ± 0.50	WISE	
J1844 – 0030	31.711	1.271	603.2	12	10.41 ± 3.12	Y	31.881	1.417	3.40 ± 0.40	WISE	
J1850 – 0006	32.764	0.093	655.0	2.6×10^2	8.56 ± 2.57	N	32.823	0.072	7.10 ± 0.10	WISE	
J1850 – 0026	32.407	0.066	947.0	46	11.10 ± 3.33	N	32.423	0.077	[2.50, 11.30]	WISE	
J1852 + 0031	33.523	0.017	787.0	3.6×10^2	9.58 ± 2.87	N	33.507	-0.002	$8.80 \pm 3.00^{\dagger}$	WISE	
J1852 + 0056g	33.853	0.249	905.7	85	11.65 ± 3.49	N	33.914	0.111	< 6.89	HH14	
J1852 – 0127	31.706	-0.802	427.9	57	7.14 ± 2.14	N	31.650	-0.649	$5.49 \pm 0.39^{\dagger}$	HH14	
J1853 + 0505	37.650	1.956	279.0	2.2×10^2	9.13 ± 2.74	Y	37.642	1.192	$1.88 \pm 0.08^{\dagger}$	WISE	
J1853 + 0545	38.354	2.064	197.9	21	6.52 ± 1.96	Y	38.123	1.660	[2.29, 10.60]	WISE	
J1854 + 0131g	34.638	-0.004	474.9	6.3×10^2	7.48 ± 2.25	N	34.932	-0.018	2.11 ± 0.60	HH14	
J1855 + 0205	35.281	0.007	867.3	16	11.65 ± 3.49	N	35.349	0.005	[3.20, 10.10]	WISE	
J1855 + 0422	37.314	1.052	455.6	54	10.95 ± 3.28	Y	37.642	1.192	$1.88 \pm 0.08^{\dagger}$	WISE	
J1856 + 0113	34.560	-0.497	96.1	1.6×10^{-3}	3.30 ± 0.99	Y	34.757	-0.669	2.99 ± 0.40	WISE	
J1856 + 0245	36.008	0.057	623.5	18	9.01 ± 2.70	N	35.663	-0.030	2.11 ± 0.60	HH14	
J1856 + 0404	37.128	0.745	341.3	13	6.77 ± 2.03	N	37.642	1.192	$1.88 \pm 0.08^{\dagger}$	WISE	
J1857 + 0210	35.586	-0.393	783.0	27	10.94 ± 3.28	N	35.588	-0.489	2.11 ± 0.60	HH14	
J1857 + 0212	35.617	-0.390	506.8	7.9	8.00 ± 2.40	Y	35.588	-0.489	2.11 ± 0.60	HH14	
J1857 + 0526	38.438	1.187	464.8	25	12.23 ± 3.67	Y	37.642	1.192	$1.88 \pm 0.08^{\dagger}$	WISE	
J1858 + 0215	35.725	-0.493	702.0	63	10.14 ± 3.04	N	35.588	-0.489	2.11 ± 0.60	HH14	
J1858 + 0346	37.083	0.182	386.0	42	7.00 ± 2.10	N	37.032	0.139	–	WISE	multiple
J1901 + 0156	35.818	-1.367	105.4	2.1×10^{-2}	3.23 ± 0.97	Y	35.673	-0.847	2.11 ± 0.60	HH14	
J1901 + 0331	37.213	-0.637	402.1	1.3	7.29 ± 2.19	N	37.370	-0.367	[2.56, 10.40]	WISE	
J1901 + 0716	40.569	1.056	252.8	0.20	5.47 ± 1.64	N	40.160	1.510	> 1.77	HH14	
J1903 + 0135	35.727	-1.955	245.2	0.24	3.35 ± 1.00	N	36.289	-1.686	1.80 ± 0.50	HH14	
J1907 + 0740	41.613	-0.102	332.0	0.24	6.85 ± 2.06	N	41.379	0.037	> 4.12	HH14	
J1910 + 0534	40.056	-1.668	484.0	25	21.25 ± 6.38	Y	39.904	-1.331	2.10 ± 0.60	HH14	multiple

Table A1 continued

Table A1 (*continued*)

Pulsar							H II Region				
Name	l	b	DM	τ	D	Method	l	b	D	Ref.	Notes
	($^{\circ}$)	($^{\circ}$)	(pc cm^{-3})	(ms at 1 GHz)	(kpc)		($^{\circ}$)	($^{\circ}$)	(kpc)		
J1913 + 1000	44.285	-0.194	422.0	22	7.86 ± 2.36	N	44.379	-0.326	6.10 ± 1.30	WISE	
J1916 + 1030	45.099	-0.638	387.2	18	8.64 ± 2.59	N	45.002	-0.610	6.00 ± 1.10	WISE	
J1924 + 1631	51.405	0.318	518.5	49	13.98 ± 4.19	N	51.010	0.060	7.20 ± 1.20	WISE	
J1946 + 2535	61.809	0.283	248.8	4.5	8.30 ± 2.49	Y	61.467	0.380	3.90 ± 0.10	WISE	
J2005 + 3411g	71.274	1.239	489.0	43	22.75 ± 6.83	N	71.312	0.828	> 2.66	HH14	
J2013 + 3845	75.930	2.476	238.2	0.13	8.43 ± 2.53	N	75.460	2.430	1.20 ± 0.50	HH14	
J2021 + 4024g	78.157	2.107	680.5	74	25.00 ± 7.50	Y	78.698	1.902	$1.50 \pm 0.10^{\dagger}$	WISE	
J2022 + 3842	76.888	0.960	429.1	55	22.06 ± 6.62	N	77.402	0.841	$1.50 \pm 0.10^{\dagger}$	WISE	
J2022 + 3845g	76.906	1.015	487.5	1.8×10^2	21.48 ± 6.44	N	77.402	0.841	$1.50 \pm 0.10^{\dagger}$	WISE	
J2029 + 3744	76.898	-0.727	190.7	4.9×10^{-2}	6.33 ± 1.90	N	77.402	0.841	$1.50 \pm 0.10^{\dagger}$	WISE	
J2030 + 3944g	78.625	0.294	937.4	1.0×10^2	25.00 ± 7.50	Y	78.689	0.355	$1.50 \pm 0.10^{\dagger}$	WISE	
J2052 + 4421g	84.833	-0.168	547.0	81	25.00 ± 7.50	Y	85.325	-0.788	$1.50 \pm 0.10^{\dagger}$	WISE	S117
J2108 + 4441	86.909	-2.012	139.8	0.11	4.96 ± 1.49	N	85.325	-0.788	$1.50 \pm 0.10^{\dagger}$	WISE	S117

NOTE—Pulsar name, Galactic coordinates, DMs, scattering time (τ) in ms at 1 GHz, distance (D), and the method used to derive the pulsar distance (P for parallax, Y for YMW16, and N for NE2001). For YMW16 and NE2001, 30% distance errors are shown. For H II regions we show Galactic coordinates, distances, and the corresponding catalog reference (HH14 for Hou & Han 2014 and WISE for Anderson et al. 2014). H II regions with parallax distances are indicated by a \dagger . Distance lower limits correspond to cases where HH14 only reports a near kinematic distance but no kinematic distance ambiguity resolution. Kinematic distances without an ambiguity resolution (e.g. from HI or H₂CO) are shown as a range spanning the near to far distances. In these cases we show intersections for pulsars with estimated distances greater than the near distance, although we note that these intersections should be treated with caution. The Notes column indicates H II region names where possible, and pulsars for which multiple H II regions may be relevant are noted as “multiple.”

B. PULSARS WITH EXCESS SCATTERING

We have identified ~ 30 pulsars with significant scattering excesses and deficits from the mean τ -DM relation for the pulsar population (§3.2). Table B2 lists these outliers, their properties, and the foreground structures that may be related to their scattering excesses and deficits.

Table B2. Pulsars with Significant Scattering Excess or Deficit

PSR	l ($^{\circ}$)	b ($^{\circ}$)	DM (pc cm $^{-3}$)	τ (ms at 1 GHz)	Candidate Foreground Structure
$\tau > 2\sigma$ from Mean τ -DM Relation					
J0450–1248	211.075	–32.629	37.0	0.029	S276; maybe Orion-Eridanus superbubble
J0502+4654	160.363	3.077	41.8	0.085	Supernova Remnant (G160.9+02.6)
J0540–6919	279.717	–31.516	147.2	1.8	Supernova Remnant (SNR 0540–693)
J0646+0905	204.271	3.051	147.9	10.0	H II Region (S273)
J0835–4510	263.552	–2.787	67.8	0.049	Gum Nebula
J1514–5925 \dagger	320.284	–1.482	192.5	16	Multiple H II Regions
J1550–5418 \dagger	327.237	–0.132	830.0	4.3×10^3	Multiple H II Regions
J1643–1224 \dagger	5.669	21.218	62.4	4.9×10^{-2}	H II Region (S27)
J1730–3350	354.133	0.090	261.3	27.3	H II Region (G354.175–00.062)
J1812–1718 \dagger	13.109	0.538	251.4	31	H II Region (S40)
J1819–1114	19.291	1.857	309.7	51	H II Region (S54)
J1833–0559 \dagger	25.514	1.321	346.7	1.8×10^2	H II Region (IRAS 18316–0602)
J1834–0731	24.288	0.366	288.3	122	Multiple H II Regions
J1841–0500 \dagger	27.323	–0.034	532.0	2.2×10^3	H II Region (G027.281–0.132)
J1849–0014g	32.505	0.321	346.6	73	...
J1849+0127	34.034	1.043	207.0	9.7	...
J1853+0505 \dagger	37.650	1.956	279.0	2.2×10^2	H II Region (G037.642+1.192)
J1853+0545 \dagger	38.354	2.064	197.9	21	H II Region (G038.123+1.660)
J1854+0131g \dagger	34.638	–0.004	474.9	6.3×10^2	H II Region (G034.932–0.018)
J1859+0601	39.245	0.903	272.4	125	H II Region (G039.283+00.865)
J1905+0616	40.069	–0.169	256.1	27	H II Region (G039.294–00.311)
J1919+1745	51.897	1.987	142.3	2.9	...
J1920+1110	46.152	–1.199	188.4	25	...
J1921+1419	49.058	0.021	91.6	8	H II Region (W51)
J1949+2306	59.931	–1.423	196.3	5.4	H II Region (S86)
J1953+2732	64.205	0.059	194.2	21	...
$\tau < 2\sigma$ from Mean τ -DM Relation					
J0953+0755	228.908	43.697	2.9	1.1×10^{-8}	Local Bubble
J1017–5621	282.732	0.341	438.7	0.11	...
J1709–4429	343.098	–2.686	75.6	3.6×10^{-5}	Pulsar Wind Nebula (G343.1–2.3)
J1932+2220	57.356	1.554	218.9	0.006	...

NOTE—Pulsars that have τ more than 2σ deviant from the mean τ -DM relation (§3.2), and the candidate structures that may explain their scattering excesses and deficits. Pulsars positively identified as intersecting H II regions by our selection criteria are indicated by a \dagger . Scattering deficits could be explained by underdense voids along the LOS or dense structures close enough to the pulsar that they contribute excess DM but no significant scattering.